A Low-Field NMR Tool for Soil Moisture

Von der Fakultät für Mathematik, Informatik und Naturwissenschaften der
RWTH Aachen University zur Erlangung des akademischen Grades
eines Doktors der Naturwissenschaften genehmigte Dissertation

vorgelegt von

M. Sc.

Oscar Elías Sucre

aus Baruta, Venezuela

Berichter: Universitätsprofessor Prof. Dr. Bernhard Blümich

Universitätsprofessor Prof. Dr. Wolfgang Stahl

Tag der mündlichen Prüfung: 9. Mai 2011

Die vorliegende Arbeit wurde in der Zeit von Oktober 2006 bis Dezember 2010 am Lehrstuhl für Makromolekulare Chemie der Rheinisch-Westfälischen Technischen Hochschule in Aachen angefertigt. Herrn Prof. Dr. B. Blümich danke ich für die Übernahme der wissenschaftlichen Betreuung dieser Promotionsarbeit. Für die freundliche Übernahme des Koreferats danke ich Dr. Andreas Pohlmeier aus der Forschungszentrum Jülich.

Gedruckt mit Unterstützung des Deutschen Akademischen Austauschdienstes

Esta tesis doctoral esta dedicada al botánico suizo

Henri François Pittier (1857-1950)

quien llego a mi querida patria, Venezuela, en 1916
a hacer ciencia, algo en aquel entonces nuevo y desconocido,
pero precisamente por ello, útil y necesario.

Contents

Chapter 1

Introduction

Soils are recognized as an important factor for the food production and for the balance in many ecosystems. In areas where water is scarce, the need to improve its usage has sparked the research of flow in soils, setting the stage for the development of the young science of soil hydrology. Nowadays, as the demand for reliable on-field characterization of soils grows [San1], the realization of heterogeneity in the soil features has fuelled the development of experimental techniques and theoretical models, which; with the help of computational tools of analysis, may elucidate the inherent character of the soil under research. Though they are far from having reached a mature stage yet, firm advances in both can be presented nowadays, as the **chapter 2** further explains. For this reason, the science of soil hydrology is experiencing a promising time in the achievement of its long-term scientific goals.

By the other hand, Nuclear Magnetic Resonance (NMR) performed at highly inhomogeneous, low magnetic fields is also experiencing a flourishing time nowadays mainly due to the fact that it is stayed unnoticed to many researchers until the pioneering work of Jasper Jackson in 1980 [Jac1]. He actually was the first person to perform an NMR measurement in *ex-situ* geometry of the magnet, i.e. under the philosophy of bringing the sensor to the sample and not viceversa, as usually it had been the case before. Posteriorly, when it was realized such sensors could provide information about fluids saturating porous media, their development received strong impetus from oilfield companies like Schlumberger and NUMAR [Kle1, Coa1], which

produced their own logging instruments. Currently there are routinely deployed in oil wells worldwide.

The measurement of soil moisture via NMR, though it was among the first applications of *ex-situ* instruments [Mat1], has not received yet an equivalent support. Nevertheless, soil hydrology has made meanwhile impressive advancements in construction a firm quantitative description of the phenomena of moisture in soils and the factors which are part of it. These advancements have been also supported by the emergence of experimental techniques such as Time Domain Reflectometry (TDR) [Rob1], Neutron Absortion [Sak1] or Electrical Impedance Tomography [Dai1]. Beyond their demonstrated utility, these techniques are not free of drawbacks: their results for soil moisture can also be adversely affected by local conditions such as ion concentration and the changes in the saturation resulting from actual presence of the sensor.

NMR certainly can play an important role in the future of experimental soil hydrology. A promising example of this is given by the NMR-sounding technique, which has successfully been applied in the search of aquifers in the last 10 years [Mej1]. In the case of low-field NMR, several advantages make it interesting in comparison to the existing techniques. The physical principle it relies on is not affected by ion concentrations in the soil and the ex-situ geometry certainly fulfills the conditions for a non-destructive measurement of soil moisture. The present dissertation constitutes a contribution in this sense: A low-field NMR sensor is presented that performs the measurement of partial saturation, the main parameter that describes the moisture in soils and also obtains information about the microscopical condition of the retained soil via Laplace analysis.

Following the actual development of research carried out, two conceptions for this instrument are presented in **chapter 4**: The NMR-SPADE, with a design based on the NMR-MOUSE®, and the NMR Slim Line Tool (SLT), with a cylindrical design inspired in the NUMAR well-logging tool [Coa1]. On the ground of considerations made for these instrument conceptions and based on the theoretical concepts presented in **chapter 3**, the SLT-tool was the chosen design to be constructed and tested. Such theoretical concepts include the phenomena of NMR in highly inhomogeneous field and the influence of totally saturated porous media on the relaxation of the NMR signal.

In **chapter 5**, a variety of outflow experiments in model soil are described to give evidence of the capability of the built sensor to monitor the flow dynamics of the retained water. In fact, using concepts of inverse analysis, it is shown how the hydraulic character of the soil can be extracted of these experimental data. From the result of these experiments, a hydraulic characterization of the model soil is obtained, paving the path to make the NMR data of partially saturated soils a routine experimental technique for the hydrologist. In this sense, the on-field measurements, presented in **chapter 6**, seemed and was to be the next natural step to do: They were carried out in a test site of the Transregio project TR32 [TR32, 2010] in Selhausen near Düren, Germany, during a eight-day long field campaign and prove that non-invasive measurement of soil moisture via NMR is possible outdoors.

So, without further preambles, the basic theory of the object of study of the built NMR instrument, that is, the dynamics of flow in partially saturated porous media, is now introduced in the next chapter.

Chapter 2

Dynamics of Soil Water

Though not having as object of study a fundamental state of matter, the physics of porous media encloses a rich variety of phenomena of basic interest and finds a broad range of applications in industry, mining and agriculture. Porous media are found in nature with certain frequency, and the fact that the most important natural resource of the world, fossil oil, lies incrusted in totally saturated porous rocks has certainly acted as an incentive for the scientific effort in this area.

On the other hand, research in partially saturated media has experienced a more recent development. It was sparked by the need to improve the usage of water in dry areas and was further driven to cope with the general objectives of the science of hydrology [Bea1]. Partially saturated soils, having water as the fluid phase, is a classical example of these media. The most primordial physical quantity in their description is the partial saturation θ, which is defined by the coefficient of the volume of water V_w retained in a certain volume V of the porous medium:

$$\theta = \frac{V_w}{V} \tag{2.1}$$

where this "certain" volume V must always be larger that the representative volume of the media (REV). The REV is the minimum volume of the medium in which the physical quantities that describe it, like density or even saturation, exhibit yet a continuous character [Bea1]. Only then can the macroscopic frame, set by the equations presented in this chapter, be taken as valid. As a natural consequence of the last definition, the value of saturation when the soil is totally saturated θ_s equals the porosity of the soil.

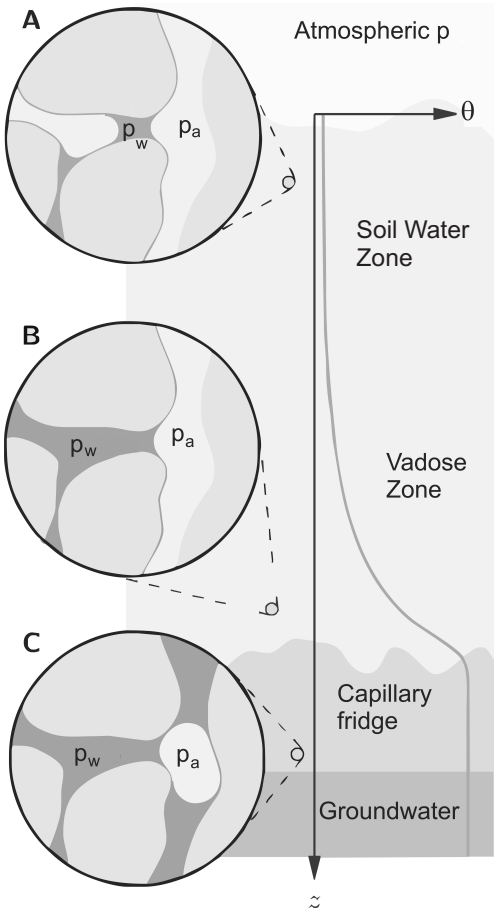

Figure 2.1: Flow regimes in partially saturated media: In the region **A**, the water phase is not continuous. The pressure p_w in water is determined mostly by the capillary pressure, and changes in the pressure p_a of air are negligible compared to those of p_w. In **B**, the water phase becomes so continuous that the p_w is given by the capillary *and* and gravity forces. This is the regime valid for the Richard equation. In **C**, the saturation θ has increased so much that the air phase is no longer continuous. p_a becomes an important driving force for water, i.e. the flows of air and water couple. Richards equation is not longer valid (Figure taken from Roth [Rot1]).

In their natural environment, subsurface water shows roughly, without any regard of either the type of soil or the meteorological conditions lying thereupon, a three-zone structure as the one displayed in Fig. 2.1. The first zone (**A**) is called the *soil water* zone and is where the water is retained mostly due capillary forces. Thereunder lies the *vadose* zone (**B**), a zone where the saturation has increased so much than the water forms a continuous phase. Under this conditions, gravitational and capillary forces determine the energetic balance of the retained water. Finally, at the bottom lies the groundwater zone or *aquifer* (**C**), corresponding to area where the soil is completely saturated. This zone can extend in depth from a few to hundred meters, depending on factors like the geology of the subsurface or the macroclimatic conditions reigning in the region. In the groundwater zone water moves in horizontal flows which develop in ranges totally different to those found in the vadose zone (hundred of km, [Rot1]).

Due to its importance in the hydraulic characterization of soils, it is the

vadose zone the area where the experimental research of this dissertation takes place. Such a characterization means to establish a model to describe quantitatively how much a soil "conducts" or "holds" water. Specially in agriculture this is an important information: Well graded soils like sandy loams [Bea1], which let water flow away under infiltration events while at the same time retain in their pore enough water to make it available for plants, exhibit in this regard a balanced behavior.

2.1 Flow in unsaturated media

In the water contained in partially saturated porous media, the capillary force plays a major role. It acts along the surface of water in the tangential direction and is originated by the difference in the inward attraction between the molecules at the interior of the liquid and those lying at the surface of the contact. It is therefore a surface-governed force, changing completely its character depending on whether or not the fluid wets porous medium.

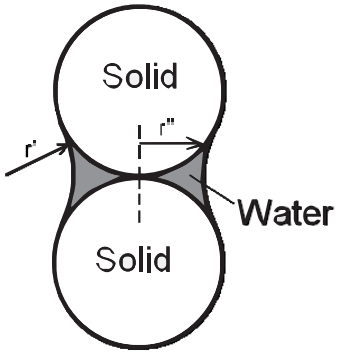

Figure 2.2: Retained water between two grains of same size.

In the case of a wetting fluid, the water phase assumes between two grains of similar size a form like that presented in the figure 2.2. For this simple example, the interface between water and air possesses clearly two principal radii of curvatures r' and r'' which are related to the value of the capillary pressure p_c through the relation $p_c{=}\sigma_{wa}(1/r' + 1/r'')$, where σ_{ws} is the interfacial tension between water and the solid matrix [Bea1]. This past equation, although represents a very simplified picture of the influence the shape of the retained water has on the pressure p_c, serves well to make a important point

common to all soils: The decrease of saturation, expressed in particular in Fig. 2.2 by a reduction of the radii of curvature r' and r'', has as a consequence an sharp increment in p_c. In fact, this capillary pressure can actually reach fairly high values for soils with small grain sizes like clay ($p_c \approx 100$ Atmospheres) when the soil is only saturated up to 5% of θ_s.

In the case of a real soil, a detailed description of the relation between p_c and the geometrical factors of the liquid interface, (and therefore the partial saturation) would be a theoretical task almost impossible to surmount. Fortunately, the concept of energy furnish us with a generalized frame that makes the relation between saturation and capillary pressure more tractable. The water pressure *head* must be then introduced, defined simply as $h = p_c/\rho_w g$ where ρ_w is the density of water and g the acceleration of gravity. The head h is an expression of the capillary energy stored in the retained water that occupies a REV of a porous medium with a partial saturation θ. In general, the functional dependance of h on the saturation θ is a proper feature of the soil, receiving in hydrology the name of *retention* function. Its determination through experimental means or its prediction through theoretical models have been research objectives in hydrology almost since its foundation as a science. Within this scientific effort, Van Genuchten T. [Van1] made an important contribution when purposed a closed-form expression for the inverse of the mentioned relationship $\theta(h)$, which reads:

$$S_e = \frac{1}{[1 + (\alpha h)^n]^{1-1/n}} \tag{2.2}$$

where S_e comes to be the relative saturation, which depends on θ in the following way:

$$S_e = \frac{\theta - \theta_r}{\theta_s - \theta_r} \tag{2.3}$$

In this last equation, θ_r represents the residual saturation and has a physical interpretation that will be clarified in short. In regard to equation 2.2, the so called *Van Genuchten* parameters like α (its inverse is the so-called air entry pressure) and n (related to the broadness of the pore size distribution of the soil) define the texture of the soil under research: Depending on its sort (sand, silt, clay or a mixture thereof) these parameter take well defined values, like those presented in the Table 2.1.

Table 2.1: Typical values for the Van Genuchten-Muallem parameters for sand, silt and loam. Taken from [Rot1].

	θ_s	θ_r	α (/cm)	n	K_o (mm/min)
Sand	0.32	0.03	0.023	4.17	1.32
Silt	0.41	0.01	0.007	1.30	0.6
Loam	0.43	0.00	0.016	1.25	0.18

Without any doubt, the retention curve $h(\theta)$ represents solely a partial aspect of the relation between the fluid and the porous medium in soils: It describes how well the soil *retains* the contained water. As mentioned before, the other aspect of these phenomena, i.e. the *conduction* of water, constitutes also another characteristic of interest. These both aspects are considered as a whole in the dynamic equation for flow in partially saturated media already established by Richards in 1931 [Bea1]:

$$\frac{\partial \theta}{\partial t} = \frac{\partial}{\partial z}\left[K\left(\theta\right)\left(\frac{\partial h\left(\theta\right)}{\partial z} + 1\right)\right], \tag{2.4}$$

where $K(\theta)$ stays for the hydraulic conductivity, a quantity naturally dependant on the partial saturation θ. The Richard equation, presented here in its 1D form, describes the evolution of the saturation $\theta(z,t)$ that depends on time t and soil depth z under the influence of gravity and capillary forces within the vadose zone. The solution manifest the hydraulic character of the soil under certain boundary and initial conditions.

Given these externally determined conditions, it is necessary to have a way to describe the conductive aspect of the soil in order to make the eq. 2.4 solvable, i.e. an analytical expression for the $K(\theta)$. Mualem [Mua1] purposed in 1976 a statistical model to calculate $K(\theta)$ based on the pore-size distribution of the soil, which, applied to the Van Genuchten model (eq. 2.2), produces also a closed form for the hydraulic conductivity:

$$K\left(S_e\right) = K_s S_e^l \left[1 - \left(1 - S_e^{\frac{1}{m}}\right)^m\right]^2 \tag{2.5}$$

where $m{=}1 - 1/n$ and l is a pore-connectivity parameter, introduced primarily by Mualem to express empirically the lack of linearity in the relation between the K and θ. Though this last parameter has been considered related to the flow-path tortuosity by Mualem himself, its exact physical interpretation is still a matter of discussion and research [Sch1, Sch2]. On the other hand, consideration of eq. 2.5 makes the significance of θ_r clear: It represents

the saturation at which the partially saturated soil no longer conducts water. This is an empirical fact that has always been observed in the experimental research and that the introduction of θ_r in the equation 3.2 permits to take into account.

The unsaturated soil hydraulic properties, $\theta(h)$ and $K(\theta)$, are in general highly nonlinear functions of the pressure head h that can be described by the Van Genuchten-Mualem model (VGM). A widely accepted model for them are provided by the Equations 2.5 and 2.2, known as the Van Genuchten-Mualem (VGM model). Together with eq. 2.4, they compose the theoretical framework to predict the behavior of saturation in the soil under any arbitrary boundary condition. It is important, however, to say the description given by them corresponds only to one side of the truth. Experimentally the saturation $\theta(z,t)$ has shown also hysteresis character, which, of course, breaks the assumed monotonous relationship between h and θ [Rot1]. This is nevertheless not a source of concern given the regime of the experiments carried out in this dissertation.

The reliable determination of $\theta(h)$ and $K(\theta)$ through experimental methods constitutes a broad front of work in hydrology. Experimental methods, established as the most accepted in this field of research and based on setups such as the Hassler, the Klute, and the Haines apparatuses, usually yield time series of data of two different sorts: $\{p_c(t_k), \theta(t_k)\}$ or $\{p_c(t_k), K(t_k)\}$, for instance [Bro1, Klu1, Oso1]. The setup presented in this dissertation produces in contrast a sole experimental type of data: A time series of partial saturations $\{\theta(t_k)\}$ measured non-invasively by NMR. The way NMR, a technique based on nuclear properties, makes possible the quantification of water in a REV is explained in the next chapter.

Chapter 3

Nuclear Magnetic Resonance

3.1 Introduction

Nuclear magnetic resonance (NMR), first known as "nuclear induction", was discovered by Felix Bloch and Edward Purcell in 1945. It is the property that some nucleus possess to emit a signal with a characteristic frequency ω_o, called the *Larmor* frequency, when exposed to a static field $\mathbf{B}_o$ and a radiofrequency (rf) field $\mathbf{B}_1$. The response of the nucleus will be maximal when the frequency ω_{rf} of the rf field equals ω_o. In other words, when the magnetic dipole of the nucleus "resonates" with the $\mathbf{B}_1$. The proportion between the Larmor frequency and the magnitude of the static field $|\mathbf{B}_o|$ happens to be a nucleus-dependant constant, known as γ. This feature of the resonance defines the basic relation of NMR:

$$\omega_o = \gamma \, |\mathbf{B}_o|$$

Two are the main conditions to achieve resonance: Equality between the rf frequency (set in laboratory) and the Larmor frequency and perpendicularity between the static and the rf fields. Since this dissertation relates to the measurement of moisture in soil exclusively, we restrict ourselves to proton resonance, i.e., γ=2.674 10^8 rad/T.sec. It is clear, however, that nuclear resonance is possible in a variety of isotopes beyond ^{1}H, like ^{7}Li, ^{19}F, ^{23}Na and ^{35}Cl, to mention some examples. It is well known that a necessary condition for the occurrence of NMR is the non-zero value of the angular momentum of the nucleus, i.e. the spin **I**. It is, therefore, a quantum mechanical property of nature, which strictly speaking must be described in a formal way by the operator formalism. Fortunately, in the case of proton (I=1/2), the operator formalism of the nuclear resonance is completely equivalent to a vectorial

description. Therefore, it is useful at this point to introduce a classical vectorial quantity that perfectly serves to describe the dynamics of resonance: the magnetization $\mathbf{M}_o$.

Consider a population of N protons in a diamagnetic sample like water or any organic compound. The addition of the magnetic dipole of their respective spins at a temperature T well above the O K and under the presence of the static field $\mathbf{B}_o$ will manifest macroscopically as the magnetization vector $\mathbf{M}_o$ of that sample, which is described by the known relation:

$$\mathbf{M_o} = \frac{N\gamma^2\hbar^2 I\,(I+1)}{3kT}\mathbf{B_o}, \tag{3.1}$$

where k is the Boltzmann constant and $\hbar$ is the constant of Planck. The role of $\mathbf{M_o}$ in the detection of NMR is of most importance: Its change in time is in fact the quantity that the element, used to detect the resonance, senses.

A straightforward consequence of eq. 3.1 is that the higher the static field becomes, the easier will be the detection of the resonance. This an important fact from the technical point of view: It explains why it is so advantageous to perform NMR experiments in high magnetic fields: as the magnetization (and therefore the signal generated by it) accordingly grows, correlation experiments become feasible, i.e. experiments where only a fraction of the available magnetization is excited.

However, it must be pointed out that in this dissertation we are concerned to the development of an application in low-field NMR, where the signal sensed by the time-dependant vector $\mathbf{M}_o$ will be inherently much smaller. The advantages of low-field approach lies in another aspect of the technique. Since it uses permanent magnets to generate the $\mathbf{B}_o$, the experimental setup needed will in general portable and small sized. In this sense, the equation 3.1 comes to be of use as a tool for the assessment of the performance in NMR equipment [Hou1].

Equation 3.1 also offers the opportunity to introduce a quantity of importance in this work: By dividing the magnetization through the number of spins $\mathbf{M_o}/N$ we obtain a quantity, which through the defining relation $\mathbf{M_o}/N{=}\chi/\mu_o\mathbf{B_o}$ (μ_o stays for permeability of vacuum) establishes also the so called nuclear susceptibility χ. As it might be supposed, this is a dimen-

sionless, intensive property of the material under research, taking different values for water (4.04 x 10^{-9}), ethanol (3.0 x 10^{-9}) or rubber (2 x 10^{-9}), and that will in fact be of use in section 4.2.

As it has been already mentioned, the evolution of the vector $\mathbf{M}(t)$ in time describes the dynamics of the resonance, governed by the macroscopic effect of the static and rf field on the population of spins. The advantages of the vector model are however not merely descriptive. It permits also the introduction of phenomenological terms that reproduce the interaction of the spins between each other (transverse relaxation T_2) and the interaction between the spins and the reservoir of energy established by the static field (longitudinal relaxation T_1). Under these assumptions, Felix Bloch proposed the equations 3.2 shortly after the discovery of NMR, furnishing so a theoretical frame for mentioned interactions.

$$\begin{aligned} \frac{dM_x}{dt} &= \gamma M_y(B_o - \omega_{rf}/\gamma) - \frac{M_x}{T_2} \\ \frac{dM_y}{dt} &= \gamma M_z B_1 - \gamma M_x\,(B_o - \omega_{rf}/\gamma) - \frac{M_y}{T_2} \\ \frac{dM_z}{dt} &= \gamma M_y B_1 - \frac{M_z - M_o}{T_1} \end{aligned} \tag{3.2}$$

These equations, expressed in a system of reference rotating with frequency ω_{rf} and where the rf field $\mathbf{B}_1$ can be simply written as $B_1\widehat{x}$, describe how the vector $\mathbf{M}$, of components (M_x, M_y, M_z) and initially at equilibrium with the value $M_o\widehat{z}$, evolves under the influence of the static field, the rf field and the relaxation terms T_1 and T_2. The Bloch equation are the basic tool to understand spin manipulation via pulsed fields and are of most importance in NMR.

Due to the averaging effect of the tumbling movement of the molecules over the dipolar interaction among the spins, liquids samples exhibit values for the relaxation times T_2 and T_1 fairly larger than those in solids. Under this circumstance, equations 3.2 can be employed during the application of short-timed rf pulses in a relaxation-free regime. A very simple result that can be extracted from this condition is the tilting effect a rf pulse of duration t_{90} of rf field has on the magnetization $\mathbf{M}$. The tilt angle β is then given by the expression:

$$\alpha = \gamma \left|\mathbf{B}_1\right| t_{90} \tag{3.3}$$

Since the maximum resonance signal will be received when the tilt angle β reaches a value of 90°, it is the common practice in NMR to set the duration of the pulse to do so. The moment in which the magnetization $\mathbf{M}$ is effectively tilted is a special one: Only then, all the spins are perpendicular to the static field $\mathbf{B}_o$ and instantaneously exhibit a feature of great importance in NMR: Coherence, that is, the spins possess all the same quantum state for a short time after off-switching the pulse.

Due to many reasons, the coherence cannot be maintained in time, leading to a decay in the oscillating magnetization $\mathbf{M}$. The so-generated signal is called the "free induction decay" (named FID, see fig. 3.1) of the nucleus. General speaking, the decay of the FID is at first order governed by the inhomogeneities of the static field and at second order by other interactions associated properly to the sample. This is a circumstance that can be regarded as unwished since, if NMR is to be applied as tool to pursue research on materials, the researcher is mostly interested in the influence the nature of the sample has on the signal and not in any field-related effect. Fortunately, Erwin Hahn found few years after the discovery of NMR a way to overcome this difficulty, the well known spin echoes.

3.2 Spin echoes

As mentioned, inhomogeneity of the static field can screen the effect that the sample-related interactions have on the FID signal. So ways to circumvent this circumstance were always wished from the early days of NMR. Erwin Hahn was the first person to realize that the loss of coherence due to field homogeneity can be reversed by a further rf pulse, and showed that the strongest signal was obtained when this second pulse, applied a time $\tau_E/2$ after the first one, corresponded to tilt angle of 180° [Hah1]. The sequence 90°-180° pulse is therefore called "Hahn sequence", shown in the Fig. 3.1, and causes the emergence of spin echo SE at a time τ_E after the first pulse. The convenience of the word "echo" to name this phenomena is then obvious: As the first experiments pointed out, the signal arose at a the time $\tau_E/2$ after the 180° pulse. This time actually equals the lapse between previously applied 90 and the 180 pulses. Hence, and citing the words Hahn used in his

pioneering article, the population of spins seemed in regard to application of rf pulses to possess some kind of "memory" when responding to the pulses.

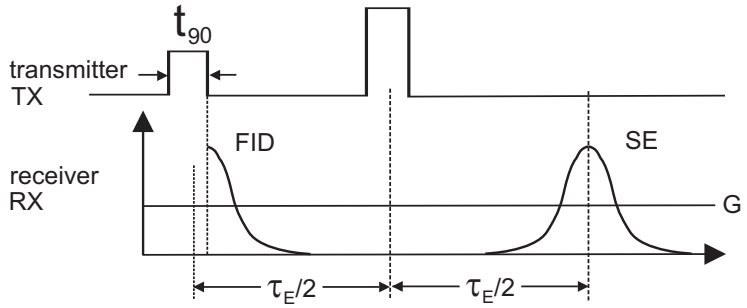

Figure 3.1: Hahn sequence. The Free Induction Decay and the Spin Echo are despicted.

Nowadays it is clear that this "memory" can be fully understood in terms of evolution of coherence. During the first stage of the sequence (between the 90° and the 180° pulses) the field inhomogeneity induces phase shifts in the evolution of the magnetization which can be inverted by the 180° pulse. Hence, all the phase shifts are balanced by the time the echo emerges. It is, furthermore, a quite fortunate circumstance that the sequence works even in fields of very high inhomogeneity, i.e. under a permanent gradient G. This makes possible the reliable acquisition of NMR signals in low-field equipment like the NMR-MOUSE or the oilfield logging tools.

There are, however, other mechanisms of loss of coherence which gain importance once the influence of field inhomogeneity has been wiped out. In the case of liquids (what this dissertation concerns) they are the diffusion movement of the water molecule and the proper transverse relaxation T_2. For this reason, the maximum amplitude of the echo SE can never reach the initial amplitude of the FID, since during the echo time τ these mechanism has been acting on the evolution of coherence. Their effect is described in the equation 3.4, which expresses the magnitude of the magnetization M at the echo time τ_E in terms of the field inhomogeneity, given at first order by a constant gradient g, the coefficient of self-diffusion D and the initial amplitude M(0) [Sch3].

$$M(\tau_E) = M(0) \exp(-\tau_E/T_2) \exp(-\gamma^2 g^2 \frac{1}{12} D \tau_E^3) \tag{3.4}$$

Although this sequence allows to overcome the loss of coherence due to

field inhomogeneity, the researcher, still willing to measure a constant like T_2 in liquid samples, must also face additional screening effect the diffusion has on the measured relaxation. In a natural extension of the Hahn sequence, Carr and Purcell [Car1] purposed a sequence that helps to quantify the influence of diffusion on the relaxation, making possible the measurement of the T_2 indirectly. Later Meiboom and Gill [Mei1] brought forth the development of this sequence by introducing a phase cycling in the rf pulses that also compensates loss of phase originated by the inhomogeneity in the rf fields. The resulted sequence, therefore called Carr-Purcell-Meiboom-Gill, has a capital importance in low field NMR: It proved crucial for enhancement of the signal-to-noise ratio in the imaging application of the NMR-MOUSE [Cas1] and it is also of routine use in well logging applications [Coa1].

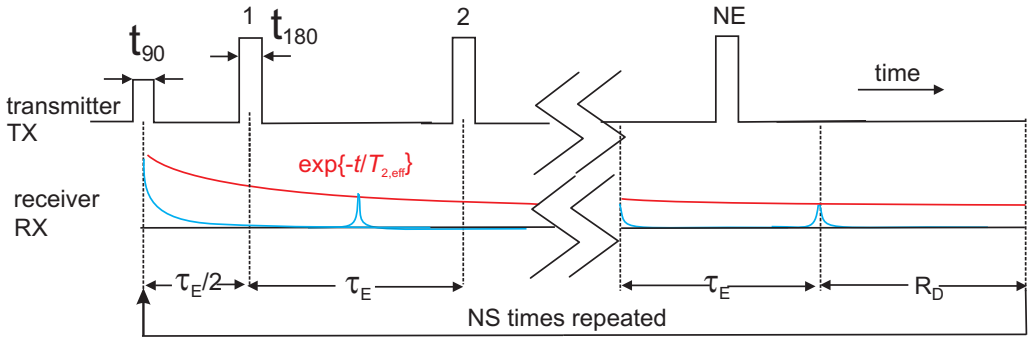

Figure 3.2: Carr-Purcell-Meibom-Gill rf pulse sequence. Figure adapted from [Blü1].

Essentially, the sequence consist in the sequential application of NE refocusing pulses (fig. 3.2) with the in-between emerging echoes acquired at time $n\tau_E$, where n is the echo number. The sequence is usually repeated a number of times NS. The total series of spin echoes constitutes a signal with a decay described a magnetization $M(n\tau_E)$ by the equation 3.5, a natural extension of eq. 3.4.

$$M\left(n\tau_E\right) = M\left(0\right)\exp\left(-n\tau_E/T_2\right)\exp(-\gamma^2 g^2 D\left(n\tau_E\right)\frac{1}{12}\tau_E^2) \tag{3.5}$$

So, by changing the echo time τ_E the weight of the diffusion term in the decay can be controlled, permitting by extrapolation of τ_E to zero a measurement of the T_2 constant in liquids.

Up to now, we have introduced concepts in NMR developed from a time in which as a technique, it was confined to indoor laboratories and performed with bulky and heavy equipment. This is, however, not the direction to which this dissertation is aimed. In general and thanks to their portability, low-field equipment is convenient for on-field applications, being many of these instrument built on *ex-situ* geometry. As a price to be paid for such a philosophy of design, their operation entails the unavoidable circumstance of detecting the NMR signal in highly inhomogeneous fields. It is important, for this reason, to delineate some key features NMR exhibites under this condition, due to their utility in the design phase of the two main instrument considered in this dissertation.

3.3 NMR in inhomogeneous fields

Hürlimann et. al [Hür1] presented in their insightful article a theoretical study of the temporal evolution of the magnetization during a CPMG pulse sequence under highly inhomogeneous fields $\mathbf{B}_o$ and $\mathbf{B}_1$. In the coming paragraphs, some ideas of their study will be presented, ideas which are also of great importance for this work.

Consider the most general case where the static $\mathbf{B}_o$ and rf $\mathbf{B}_1$ fields occupy a semi-infinite volume with an known spatial dependance. It is at this level convenient to introduce the effective field $\mathbf{B}_{1,c}$ that tilts the magnetization when the pulse are applied, i.e. the component of $\mathbf{B}_1$ that is both orthogonal to $\mathbf{B}_o$ and polarized circularly, which is expressed by the following relation:

$$\mathbf{B}_{1,c} = \frac{1}{2}\Big[\mathbf{B}_1 - \mathbf{B}_o \frac{\mathbf{B}_1 \cdot \mathbf{B}_o}{\mathbf{B}_o \cdot \mathbf{B}_o}\Big] \tag{3.6}$$

Given the most general spatial dependance of the static and rf fields, the two main conditions for resonance, mentioned already in the introduction, will only comply totally in a certain surface and partially in a space surrounding this surface. To describe how well this compliance, the definition of the offset frequency:

$$\Delta\omega_o = \gamma\,|\mathbf{B_o}| - \omega_{rf} \tag{3.7}$$

and the frequency equivalent of the effective tilting rf field

$$\omega_1 = \gamma\,|\mathbf{B}_{1,c}| \tag{3.8}$$

comes to be of use. These definitions establish then a new set of variables to describe the resonance. To make their utility evident, consider the following example: Taking into account also eq. 3.3, a point in space, where the spin are on-resonance and the rf pulse of duration t_{90} accomplish to tilt the magnetization $\mathbf{M}$ 90 degrees, is represented by the pair of values $(\Delta\omega_o, \omega_1)=(0, \pi/t_{90})$. So all the places in space where the main conditions for resonance are totally fulfilled will be depicted in the space $\Delta\omega_o - \omega_1$ by this sole point. As the reader might intuit, the usage of these variable space furnishes a theoretical frame where the resonance in highly inhomogeneous fields finds almost seamlessly its natural expression.

Now the evolution of the unitary magnetization $\mathbf{m}$ during a CPMG sequence can be better considered. Exposed to multiple manipulations carried out by the rf pulses, its evolution takes place numerous coherence pathways. Although the structure of these pathways can become quite complicated, since it grows with the number of pulse applied [Kim1], it has been shown that the temporal evolution of $\mathbf{m}$ can asymptotically be described as a simple rotation around an effective axis $\widehat{n}_B$. The concept of the effective axis of rotation is indeed very useful as it helps to conceptualize the behavior of the resonance locally.

In order to bring these ideas forward, a convention, implicitly introduced in eq. 3.2 and assumed throughout this dissertation, must be now stated: the direction of the static field $\mathbf{B}_o$ determines the local z-axis and the field $\mathbf{B}_{1,c}$ does the same for the local x-axis. Hence, the most general field maps $\mathbf{B}_o$ and $\mathbf{B}_1$ defines a the frame of reference that changes point to point in the whole volume of interest. The projection of the effective axis of rotation $\widehat{n}_B$ onto the local frame of reference (n_x,n_y,n_z describes the effect the local fields have on the resonance point by point, independent of the shape the latter might have: An axis of rotation that lies mostly in the z-axis ($\widehat{n_B} \approx \widehat{n_z}$) means that the local magnetization has been barely affected by rf field $\mathbf{B_1}$. On the other hand, if the $\widehat{n}_B$ is projected away from the z axis, the more effective the fields has been at that certain point to induce resonance.

Another useful concept is the nutation frequency Ω, i.e. the angular frequency of the magnetization during the active period of the rf pulse.

$$\Omega = \sqrt{\Delta\omega_o^2 + \omega_1^2}$$

So, with the use of the definitions for Ω, $\Delta\omega_o$ and ω_1, and taking into account the temporal parameters of the CPMG sequence (Fig. 3.2), its final effect on the unitary magnetization **m**, initially lying parallel to z axis, can be calculated. The result $m_{\infty,y}$, projected over the y-axis, corresponds to the component of **m** that effectively induces NMR signal in the coil, as a consequence of the principle of reciprocity [Hou1]. It is described by the following formula:

$$m_{\infty,y} = \frac{\omega_1}{\Omega} \frac{sin\left(\Omega t_{90}\right)}{1 + \left[\frac{\Omega}{\omega_1} sin\left(\Delta\omega_o/2\right) cot\left(\Omega t_{180}/2\right) + \frac{\Delta\omega_o}{\omega_1} cos\left(\Delta\omega_o t_E/2\right)\right]^2} \quad (3.9)$$

Equation 3.9 is a very general one, since it is expressed on the space of variables ($\Delta\omega_o$,ω_1). It is also, for the same reason, a powerful equation indeed. To illustrate this point, consider the Fig. 3.3, where the equation 3.9 is evaluated over the mentioned space for a CPMG pulse sequence of parameters t_{180}=35 μsec and τ_E=130 μsec. The election of these parameters is in fact not arbitrary, as appendix A will later show.

In this figure the nine contour lines of $m_{\infty,y}$ for values between 0.8 and -0.8 are depicted. As expected, the points where the magnetization is tilted 90° and 270° ($m_{\infty,y}$=1,-1) are represented by the coordinate pairs (0,π/t_{180}) and (0,$3\pi/t_{180}$).

Though its generality, it is important to place this figure in the right context to avoid misuse. When the scaling of the rf field is made in π/t_{180} units, it is assumed inherently that the arrangement made by the rf coil, the tank circuit and the power amplifier will always supply power enough to tilt the magnetization at the point where the resonance occurs. Depending on the actual value of ω_{rf}, such a condition might be hard to achieve experimentally for certain points in space, so care must be taken when conferring a interpretation to the Fig. 3.3 in the light of a given static field geometry.

There are other features of the Fig. 3.3 which deserve to be commented. The bath-like structure of the contour lines is strongly dependent on the values of t_{180} and τ_E. Furthermore, the width of this structure around the point of tilt magnetization (0,π/t_{180}) is inversely proportional to the length of the refocusing pulse t_{180}. The structure represents all the spins with a

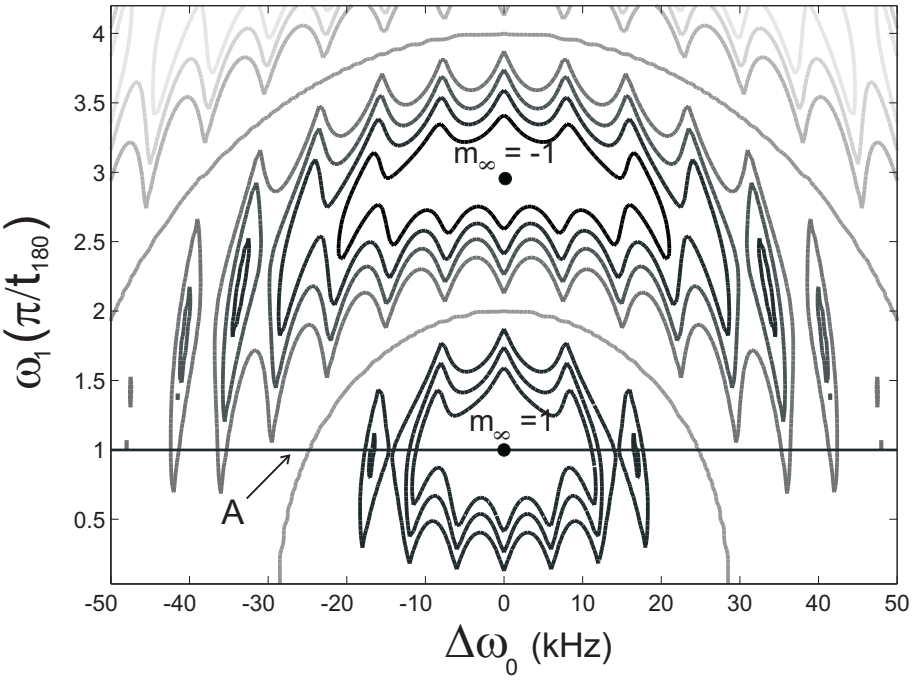

Figure 3.3: Coherence map for $m_{\infty,y}$ calculated to a CPMG pulse sequence in inhomogeneous fields with parameters t_{180}=35 μsec and τ_E=130 μsec.

magnetization that has been partially tilted by the sequence. If for a certain sensor of the field maps $\mathbf{B}_o$ and $\mathbf{B}_1$ are given, the evaluation of this structure in the functional relation between the $\Delta\omega_o$-ω_1 space and the space (x,y,z) will determine the sensitive volume V of the sensor. As a consequence, the election of t_{180} defines the size of the sensitive volume. Precisely in this point lies the conceptually most important difference between NMR in homogeneous and in inhomogeneous fields: Whereas in homogeneous fields the length of the pulse determines the tilt of the magnetization only, in inhomogeneous fields each pulse of finite width is selective in space, affecting the signal not only through the tilt of the magnetization but also through the amount of spin excited. Due to importance of this issue for the performance of low-field sensors, an additional discussion in relation to this point is lead in appendix A.

Another feature of relevance that NMR depicts under these circumstances is the inhomogeneous character of the effective axis of rotation $\widehat{n}_B$ depicts,

thus affecting the effective relaxation time $T_{2,eff}$ with which the NMR signal decays. As a consequence, $T_{2,eff}$ comes to be the result of the linear combination of the T_1 and T_2 values with a weighting factor determined by $\widehat{n}_B$. In concrete terms:

$$\frac{1}{T_{2,eff}} = \frac{1}{T_2} + \langle n_z^2 \rangle \Big(\frac{1}{T_1} - \frac{1}{T_2} \Big) \tag{3.10}$$

where $\langle n_z^2 \rangle$ stays for the average over the sensitive volume of the squared z-component of $\widehat{n}_B$, logically calculated over a global frame of reference (not locally determined). The effect expressed by equation 3.10 should be intuitively clear: The magnetization $\mathbf{m}$, now partially tilted point to point, relaxes in a mode that is a mixture of the two main modes T_1 and T_2. The more efficiently has the magnetization been tilted in given point ($n_z \approx 0$) the more the relaxation will be governed by the T_2 solely.

General speaking and taking into consideration the most general field map a low-field NMR sensor may have, the diffusion effects will also intermingle with this mixture of relaxation modes. This fact will be of importance in the interpretation of the relaxation spectra acquired with the constructed NMR Slim-line Logging Tool for research on soil, as will be explained in the Section 4.3. The mathematical tool to produce these spectra, the discreet inverse Laplace transformation, must be therefore introduced in the next section.

3.4 Relaxation in NMR

In the process of losing coherence, the population of spins lying within the sensitive volume may relax at different rate due to multiple reasons. In the acquired signal all these rates superpose, manifesting as the addition of several mono-exponentials, each of them characterized by a proper decay time T_k. The Inverse Laplace Discreet Transformation (ILDT), implemented through an MATLAB code developed by the New Zealand group [God1], helps to disentangle these variety of decays, producing the so called relaxation or T_2-spectra. Consider a set of discree time values t_i to which the decaying signal $S(t_i)$ is related, the ILDT transformation consists of finding a set of amplitudes A_k related to exponential functions which added together should reproduce the shape of the acquired $S(t_i)$ signal. Expressed in mathematical language:

$$S(t_i) = \Sigma_{k=1}^{N} A_k(T_k)\, e^{-\frac{t_i}{T_k}} \tag{3.11}$$

By plotting the obtained A_k against T_k is the T_2-spectra constructed, so as it has been done in the Fig. 3.4-B for the result of the ILDT transformation applied on two different NMR signals (fig. 3.4-A). Clearly two main modes of decay have been separated in both signals, and furthermore, absolute differences between the modes are also found, showing therefore the utility of the transformation in resolving features of the decay. Although a further discussion about the resolution and sensitivity aspects in the ILDT tool lies beyond the scope of this work, the interested reader is referred to the article of Song Y [Son1].

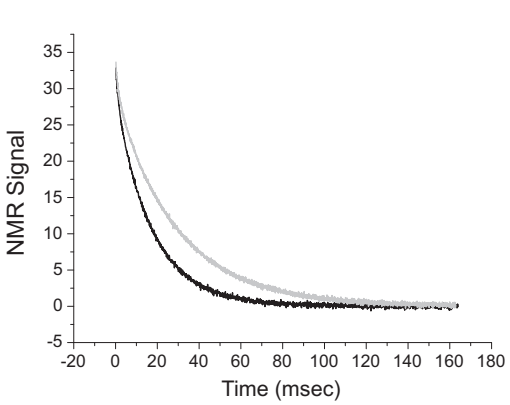

Figure 3.4: Two decaying NMR signals acquired with a CPMG sequence

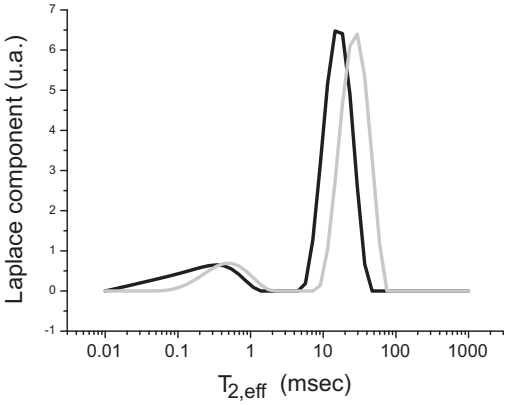

Respective T_2 spectra.

3.5 NMR in porous media

In case the fluid retained in a porous medium, another mechanism of relaxation that comes into play is the interaction between the surface of the solid matrix (that can contain traces of paramagnetic elements) and the nuclear spins. Together with this interaction, the diffusion movement of the spin can also be limited by the proper presence of the solid matrix, changing the way it affects the effective relaxation. Due to their simultaneous occurrence, interdependent nature and importance in the current research of porous media, these phenomena are nowadays object of research extensively reported in the literature [Fol1, Mit1, Hür2, Kle3, God2].

$$\frac{1}{T_{2,surf}} = \rho_s \frac{S}{V} \tag{3.12}$$

Despite this inherent complexity, the following fact has gained acceptance among NMR researchers: The influence of the porous medium has on the relaxation can be described through the Equation 3.12, which establishes the surface-induced relaxation time $T_{2,surf}$ for a spin diffusing in a pore with a surface-to-volume ratio S/V. The material specific constant ρ_s reflects the superficial density of paramagnetic trace lying on the surface of the solid matrix.

Equation 3.12 has made NMR useful for research in porous media, since it permits to obtain structural information of the porous structure in a non-destructive manner. Nevertheless, care must taken when considering the condition under which this equation actually holds: A ratio $\rho_s <r> /D$, where the $<r>$ is the average size of the pore, lower than 1, means that the diffusion of the spins within happens so rapidly that *on average* all the enclosed spins "feel" during the CPMG sequence the enhancing effect the surface has on the relaxation. Such case, called "fast" diffusion limit, corresponds to the regime in which the equation 3.12 is valid. Under this circumstance, the total influence of the diffusion, transverse and surface relaxation can be covered by adding eq. 3.12 to eq. 3.5, yielding the following equation for the effective transverse relaxation:

$$\frac{1}{T_{2,eff}} = \frac{1}{T_2} + \rho_s \frac{S}{V} + \frac{D\gamma^2 g^2 \tau_E^2}{12} \tag{3.13}$$

So presented, relaxation of NMR signal from a fluid retained in the porous medium can be studied by an *ex-situ* sensor by making use of the last equation. When the NMR signal is acquired with short echo time (take for example 200 μsec for the Schlumberger logging tool [Kle2], a design were the gradient at the sensitive volume is specially low), the diffusion term looses dominance in the effective relaxation. The obtained T_2-spectra will exhibit then a shape that is directly proportional to the pore distribution of the sample. That correlation is of great value in NMR analysis of oilfields.

In the other hand, for partially saturated soils researched with the SLT sensor developed in this dissertation, the diffusion term in the 3.13 can not be neglected anymore due to the inherently high value of the gradient found.

This is an aspect to take care of when conferring an interpretation to the relaxation spectra acquired with this sensor, and it is further developed in next chapter.

Chapter 4

An NMR Moisture Sensor for Soils

4.1 Introduction

With the aim of taking advantages of the capabilities low-field NMR has shown to analyze fluids in porous media, an instrument was envisioned to perform on-field studies in natural soils. Previously done work in this research area includes: Patented designs of instruments like those of oil companies such as Schlumberger and Halliburton [Kle1, Coa1] and also the design of the NMR-MOUSE® [Blü2]. Beyond their conceptual similarities, a circumstance differentiates the object of study in this work from the corresponding one in the mentioned designs: Whereas oil logging tools were designed to characterize porous media totally saturated, soils constitute an example of *partially* saturated media.

The pursued goals for the purposed instrument are two: First, if the sensor, whatever its final conception comes to be, is going to compete with the techniques already established in hydrology like TDR [Rob1] or Neutron Absortion [Sak1], it must also measure the partial saturation θ in a REV with similar or even better accuracy. Second, it should make use of the surface relaxation to obtain information about the porous structure of the soil. About this latter point previously done research in partially saturated soils with *in-situ* NMR instruments comes to be of help [Sti1]: In these instruments, the strength of NMR signal is specially high, making multidimensional experiments like diffusion-weighted relaxation analysis [Hür2] and surface-weighted relaxation analysis [Kle3] feasible.

It is clear, however, that the partial saturation adds another variability in the surface effect of the solid matrix, so that the interpretation of NMR data under this circumstance acquires an increased complication. Though a complete quantitative interpretation of such a NMR data, even for *in-situ* instruments, has not been accomplished, a simple fact must always be kept on mind when striving towards its construction: The more a result, extracted from NMR data, is determined by the sample solely, the more useful it will eventually be for the hydrologist or soil scientist.

In order to achieve these two goals, two conceptions in NMR instrumentation have been considered in this dissertation, one theoretically only and the other theoretically and practically: The NMR-SPADE and the NMR Slim Line Logging (SLL) tool.

4.2 The NMR-SPADE

Two are the elements which define the overall performance of an NMR sensor: The magnet that generates the static field $\mathbf{B}_o$ and the coil that produces the rf field $\mathbf{B}_1$. Therefore, the correct design of a sensor takes into consideration both of them. Under this assumption and based on the experience gained with the construction of the NMR-MOUSE®, the development of the NMR-SPADE is presented in this section. Calculations of the expected sensitivity of the instrument for different designs are performed, based on theoretical considerations conducted in the appendix A. The obtained result facilitates further decision-making in regard to the final low-field NMR instrument to be constructed.

The NMR-SPADE was intended to be rammed into the soil and should measure the NMR signal of water in soil from an sensitive volume lying 50 mm away from its outer surface. Its application field was set on multidimensional relaxation analysis and when possible, imaging.

The NMR-MOUSE® represents a good example of a low-field NMR instrument to perform reliable non-destructive analysis of materials in a *ex-situ* geometry[Blü3]. Originally conceived for applications in material science, this instrument has shown its capability to perform imaging [Per1], depth scanning with high spatial resolution [Per2], non-destructive analysis of porous

media [Sha1] and even high resolution spectroscopy[Per3]. The primordial philosophy of design in the MOUSE® follows a simple goal: The gradient of $\mathbf{B}_o$, as a degree of the inhomogeneity, must be as uniform as possible within a large volume over the sensitive side of the instrument. Beyond its simplicity, such approach entails also an important advantage when tailoring the design to the application the instrument is intended for: Designs with gradients between 32 T/m for depth scanning to 0 T/m for high resolution spectroscopy have been successfully implemented.

In its rough form, the NMR-SPADE was thought to have as dimensions: 300 x 200 x 50 mm, following the design of the MOUSE®. The arrangement of magnets comprises four permanent magnet blocks adhered to an iron plate that deforms the field lines at one side in such a way that these become more focused at the other side (See Fig. 4.1). As it can be recognized, the orientation of the magnets introduces an inherent symmetry in the $\mathbf{B}_o$ field at the center of the rectangle, which is naturally selected as the measurement spot. By taking advantage of the variability of the magnitude of the static field gradient g with the magnet design, ten different designs have been considered, searching for nothing else but the enhancement of the geometrical homogeneity of the field lines at several measurement depths.

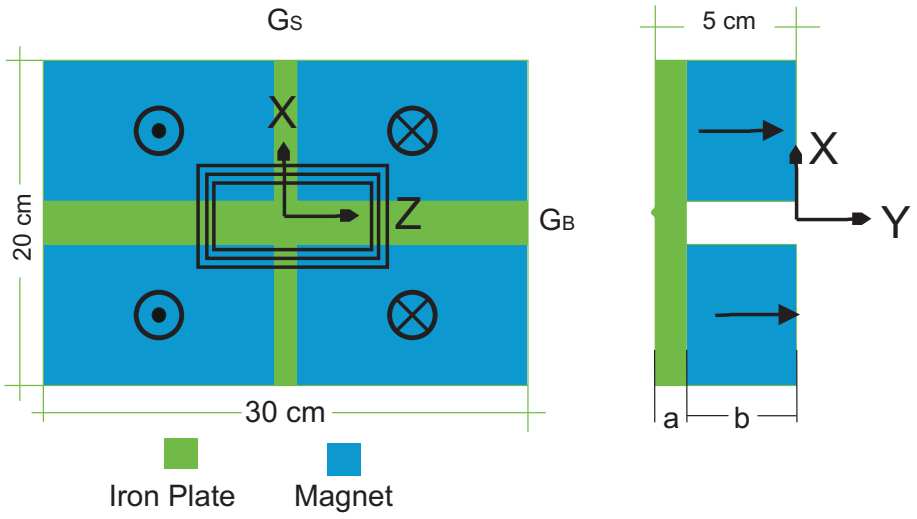

Figure 4.1: Magnet design for the NMR-SPADE. At the origin, the z-axis is parallel to $\mathbf{B}_o$.

The parameters of importance which define the considered designs are: The small and big gaps ($\mathbf{G}_S$ and $\mathbf{G}_B$) between the magnet blocks and the

thickness of the magnet **b** and the iron plate **a**. The ten considered designs are presented in the Table 4.1. Only the thickness **a** and the gap $\mathbf{G_B}$ are reported, since **a**+**b**=50 mm and the value of $\mathbf{G}_S$ is constrained by $\mathbf{G}_B$ in a way explained soon. The rf coil is represented by a black rectangle centered at the origin.

Table 4.1: Designs 1-10 for magnets in the NMR-SPADE

Design (mm)	a (mm)	G_B (mm)
D1	30	20
D2	35	20
D3	30	30
D4	35	30
D5	30	40
D6	35	50
D7	30	50
D8	35	50
D9	40	50
D10	40	40

Solutions of the magneto-static problem posed by these magnet design were obtained with the OPERA® commercial software, following the frame of reference defined in 4.1. An example of the obtained solution for design D1 is presented in the Fig. 4.2, where lines of constant amplitude are plotted.

Assuming that the uniformity in the lines of constant magnitude $|\mathbf{B}_o|$ is equivalent to an uniform gradient, careful examination of Fig. 4.2 makes evident an expected feature for this design: The lines between 4000 and 5000 gauss experience a slow change in the sign of their central curvatures, i.e. in an area between 1.7 and 0.7 cm along the Y axis. Consider the line where the central curvature does become cero: It lies approximately at the coordinate y_o 13 mm, and it is where the static fields exhibits a more regular inhomogeneity. In an equivalent depiction, the magnitude of $\mathbf{B}_o$ has been plotted in Fig. 4.3 against the X and Y coordinates surrounding this area, endorsing this affirmation further, as the change of sign in the central curvature of the magnitude lines becomes evident.

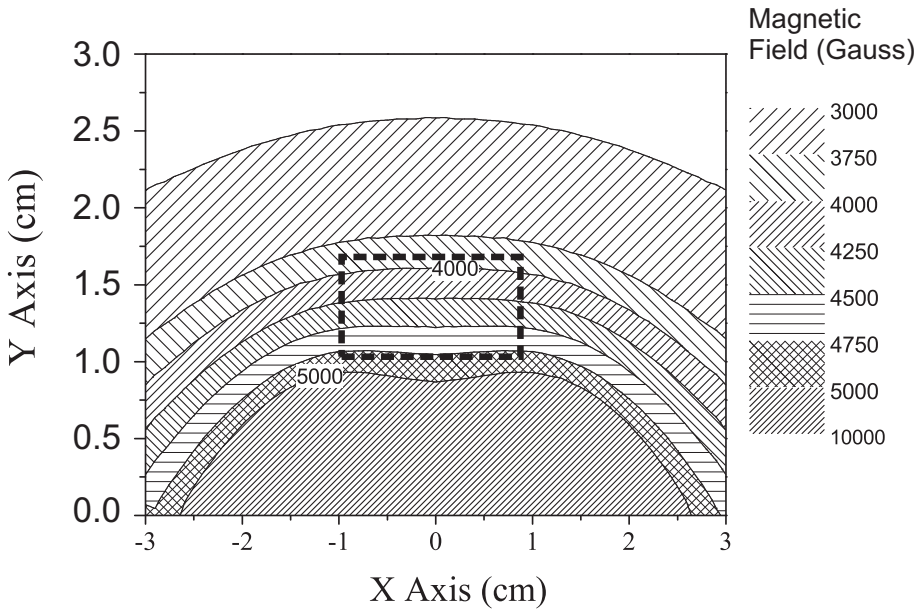

Figure 4.2: Contours of constant magnitude $|B_o|$ over the center of the magnet with design D1. XY Plane. Dashed box represents the area of homogeneous field.

The position y_o is where the sensitive volume for the design D1 must be placed: Due to the uniformity in field direction, this volume will possess, in case the sensor is constructed, a convenient flat shape. The position y_o would be in this sense the "depth" of the to-build sensor: It marks the "penetration" into the sample space and is a very important parameter for this dissertation, as it determines also the overall performance of any low-field NMR instrument. As mentioned, for the design D1, this depth equals 13 mm.

So, the origin of this enhanced uniformity in the XY plane at coordinate y_o=13 mm is the introduction of a gap G_B of 20 mm along the Z axis. The small gap G_S, defined along the X axis, plays in this sense a parallel role, but for the field in the ZY plane: For this reason it is left undefined in the definition of the designs, since it can always be adjusted to extend the found uniformity to the plane **Z**.

For the rest of designs considered, the feature of enhanced uniformity is found at certain coordinates y_o which are presented in the table 4.2, together with the corresponding values for the magnitude of $\mathbf{B}_o$ and the gradient g. These are all quantities needed for the calculation of the sensitivity.

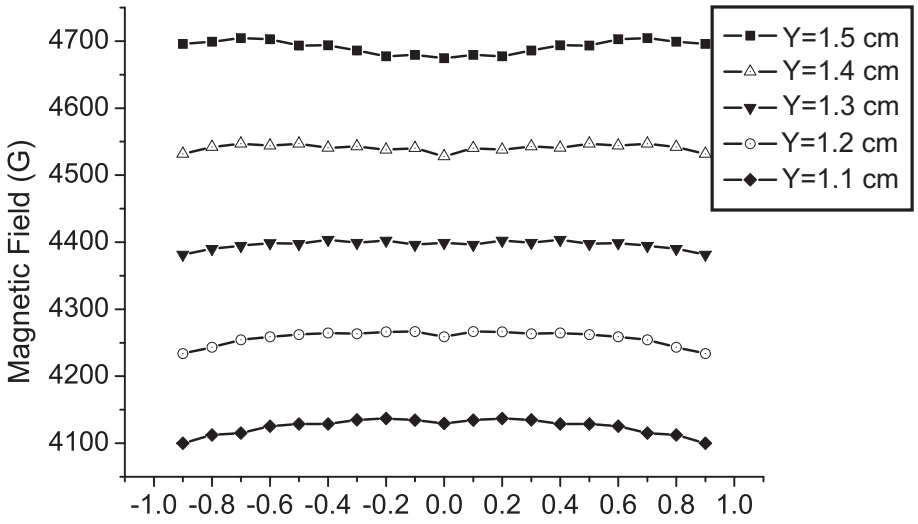

Figure 4.3: Zoomed homogeneous area for Design D1. Field magnitude in the Y plane.

Up to now, the present considerations have been turning around the static field. The rf field, responsible for the excitation of the nuclear spin, influences also the overall performance of the instrument at each depth and can be also calculated in its static form with the geometry of the rf coil to be deployed in the sensor. The "expected" sensitivity or the theoretical signal-to-noise ratio can then be evaluated with knowledge of the static and the rf fields with the help of the eq. 4.1, an expression derived in the appendix A.

$$SNR_{theo} = \frac{1}{V_{noise}} \frac{\chi}{\mu_o} B_o^2 \int_A dxdz \frac{\omega_1 (x, y_o, z)}{I} \frac{\sqrt{3}\pi}{t_{180}\gamma g} \tag{4.1}$$

where χ is the susceptibility of the material to which the spin belong, ω_1/I the spatial dependent geometrical factor that stays for the receptivity of the coil, t_{180} the pulse width that effectively refocus the magnetization at the considered depth, V_{noise} the thermal noise level present in the coil and μ_o the magnetic permeability of vacuum. This SNR_{theo} corresponds to the intrinsic ratio of NMR signal to noise, acquired with a CPMG sequence, per scan per echo. It is therefore equivalent with the operational definition of SNR:

$$SNR_{exp} = \frac{S}{\sigma} \frac{1}{\sqrt{NE \cdot NS}} \tag{4.2}$$

where noise level, σ, represents the standard deviation of S over several measurements. So, to obtain the expected sensitivities for each design, Equation

4.1 is evaluated for each depth y_o, magnitude of $\mathbf{B}_o$ and the gradient g. The reception efficiency of the coil ω_1/I is obtained from the Biot-Savart calculation of the field for a planar coil of dimensions 53 x 45 mm, made of cooper wire of diameter 1.47 mm, and with a noise level of 42 nV, (Appendix A,BIG Coil).

For an amplifier supplying 2000 W of rf power, the required pulse length t_{180} has been calculated for each depth y_o, based on experimental information obtained from a 300 W amplifier (Appendix A) and the 90° condition for the rf pulses expressed by Eq. 3.3. Results of this calculation are presented in Table 4.2, completing thus the necessary parameters for the evaluation of Eq. 4.1. The so obtained SNR_{theo} are also depicted in that Table, calculated with a MATLAB routine and supposing a semi-infinite sample of water ($\chi_W = 4.04 * 10^{-9}$ in mks units) that occupies the sensitive volume at any depth.

Table 4.2: Theoretical SNR for Designs 1 to 10

Design	y_o (mm)	B_o (T)	g (T/m)	t_{180} (μsec)	SNR_{theo}
D1	13	0.439	13.7	11.5	63
D2	16	0.40	12.3	13.5	42
D3	22	0.30	7.6	19.5	21
D4	23	0.3	7.6	20.7	18
D5	33	0.21	4.8	37.9	5.6
D6	35	0.21	4.8	42.6	4.8
D7	42	0.16	3.4	62.7	2.0
D8	53	0.13	2.4	108	0.8
D9	38	0.17	4.1	50.5	2.7
D10	30	0.23	4.8	31.8	8.2

In order to put the Figures of the Table 4.2 in context, it necessary to mention some of the experimental SNR_{exp} achieved for NMR equipment of routine use. In a high field (f_o=300 MHz) equipment SNR can reach a value of about 1000. In a Halbach magnet [Anf1] 2D relaxation experiments are performed routinely with an SNR of 200 aproximately. Following Table 4.2, an SNR of 0.8 with a depth of 53 mm is what it can be expected from a magnet design optimized for that depth and from a rf pulse with a power of 2000 W, so as the past discussion has shown. That means an enormous increment in the required time for multidimensional experiments: If an ex-

periment takes in the Halbach magnet 10 min to perform, it would need 1276 hours to make in the SPADE with the same level of noise. Once it was clear that even with optimized design of magnets and high power pulses there was a barrier set by the noise level impossible to surmount, a radical change in the conception was taken into consideration. That is, a cylindrical geometry for the magnets.

4.3 The NMR slim-line logging tool

In regard to the design most convenient to the low-field instrument, there is an additional reason, beyond the predicted low performance at large depths with the MOUSE geometry, that makes the cylindrical design more suitable for purpose intended: The slim-line logging tool (SLL tool) can perform profiling of water saturation along the soil depth (not to confuse with the depth of the sensitive volume), supplying therefore an information that reflects better the hydraulic character of the soil under research.

Being that the case, the instrument is not to be rammed but introduced into a borehole previously made in the ground. By detecting the NMR signal while moving the tool along the hole, a profile of the saturation is obtained. The borehole where the tool should move is delimited by a standard PVC tube of internal diameter 50 mm and with walls 2 mm thick. This dimension sets therefore the first constraint for the design of the tool: 48 mm was the diameter chosen for the future SLL tool. The second constraint is set by the wished depth of the sensitive volume, aimed to be 10 mm, which, although far smaller than the depths considered in the past section, still ensures the non-invasive character of the NMR measurement.

The first element to conceive in the conception phase was the body of magnets. It consist of six cylindrical magnets made . Two of the cylinder have a diameter of 48 mm and a length of 30 mm long each, and the remaining ones 38 mm diameter and 40 mm length. They are magnetized in a direction perpendicular to their axis, and are assembled with their magnetization parallel to each other.

So as it was done for the NMR-SPADE design, the static field for this

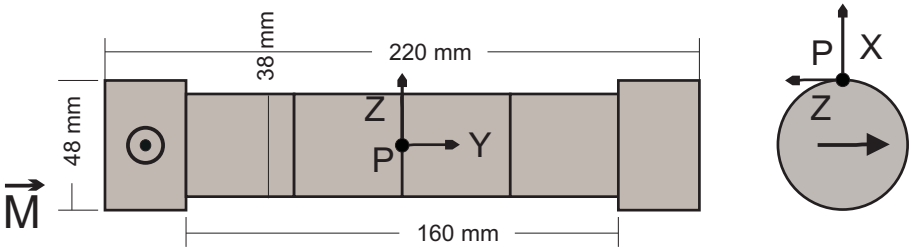

Figure 4.4: Lateral view of the body of magnet for the SLL tool. **M** stands for the magnetization vector

geometry of magnet was calculated with OPERA®, following the frame of reference given in Fig. 4.4. As can be seen, the body of assembled magnets possesses a dumbbell-like form implemented to increment the uniformity of gradient over the point P. This is a statement that the contour lines for constant magnitude of $\mathbf{B_o}$, shown in the Fig. 4.5 supports: The lines exhibit a uniformity along the Y axis from the surface of the magnet up to a radius of 39 mm (20 mm away from the surface) in a central area roughly 120 mm long. Irregularities in the contour lines are a consequence of the interpolation method that the OPERA® program applies to evaluate the field in a regular array (i.e. they are a numerical artifact) and have therefore no consequence for the validity of the present discussion. Thus, an uniformity in the gradient is gained, more or less in the same way in the field distribution in the NMR-MOUSE, that in principle should facilitates the measurement of the diffusion of the water retained in the soil. A last detail in regard to the direction of the static field should not been overseen: It varies tangentially, though the field self stays constant in magnitude with the radius and parallel to the z-axis at the point P as the Fig. 4.5 shows.

After having completed the design phase, the 6 cylindrical magnets were manufactured with a NdFeB alloy [Fur1] as depicted in figure 4.4 and with a hole of 6 mm running along their axis. This hole permits to assemble the cylinders with nuts tightened in a threaded rod running through them. The cylinder are glued together with epoxy. The rod and the hole are not shown in Fig. 4.4 for the sake of clarity, but they can be seen in Fig. 4.7. To check how well the calculation of the static field predict the actual field, the latter was measured with a Hall probe. Results are presented in Fig. 4.6 in units of Larmor frequency, showing how well they match indeed.

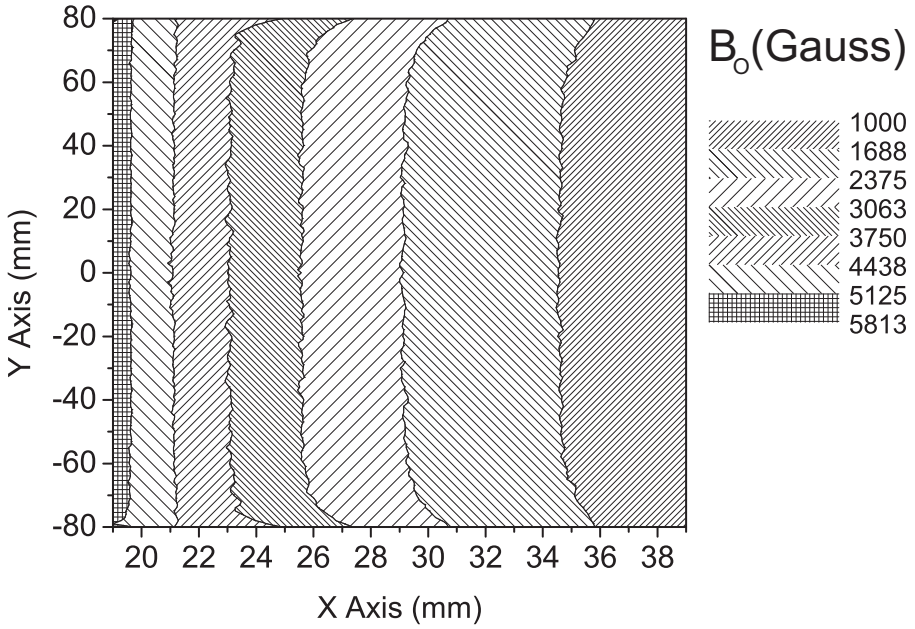

Figure 4.5: Contour lines for constant magnitude of $\mathbf{B_o}$ in the SLL tool.

The attentive reader might, at this stage of the discussion, raise the pertinent question of, given the spatial distribution of $\mathbf{B_o}$ for this cylindrical tool, whether equation 4.1 would serve also in this case to calculate the expected sensitivity SNR_{theo} at several depths. There is a circumstance that inhibit its application in this magnet design. Given the place where the rf coil is laid (point P, fig. 4.4), image currents induced by the coil at the conductive surface of the magnet cylinder detract the actual rf field $\mathbf{B}_1$ in a way that the simple integration of the Biot-Savart law does not reproduce. Hence, evaluation of eq. 4.1, that requires exact knowledge of the spatial distribution of $\mathbf{B_1}$, stands by for future refinements in the tool until this effect in the rf field can be taken into account.

The planar coil is made of copper foil 300 μm thick, creating a rectangle 50 mm long and 25 mm wide and having a conductive path 5 mm width. Once cut, the coil is laid on a curved plastic holder, assuming its curvature. Wedged perforations are made in the holder and then covered with epoxy glue. Once the glue has hardened and the holder is laid at the point P, Fig. 4.4, the coil lies 5 mm over the surface of the magnet and has therefore a radius of curvature of 48 mm, making a sole surface with the end cylinder of the magnet. The holder is attached to the body of magnet by 10 copper bands (5 at each side), as depicted in Fig. 4.7. The bands are soldered to an additional

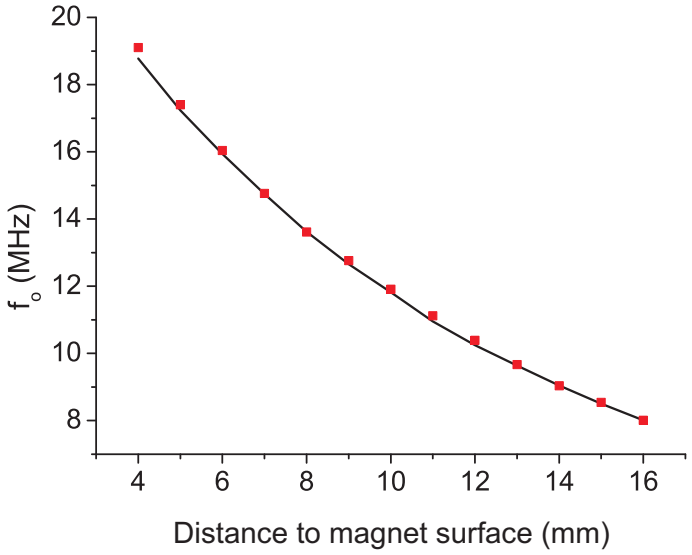

Figure 4.6: Static field in MHz, calculated (line) and measured (points).

cooper foil (that wraps the central area of the body of magnets), making the whole a solid rigid unit. This is a key factor to achieve a proper detection of the NMR signal: The magneto-acoustical ringing, a consequence of the Lorentz forces present during the rf pulse, diminishes considerably when the coil and the magnet behave as a sole body [Kle2].

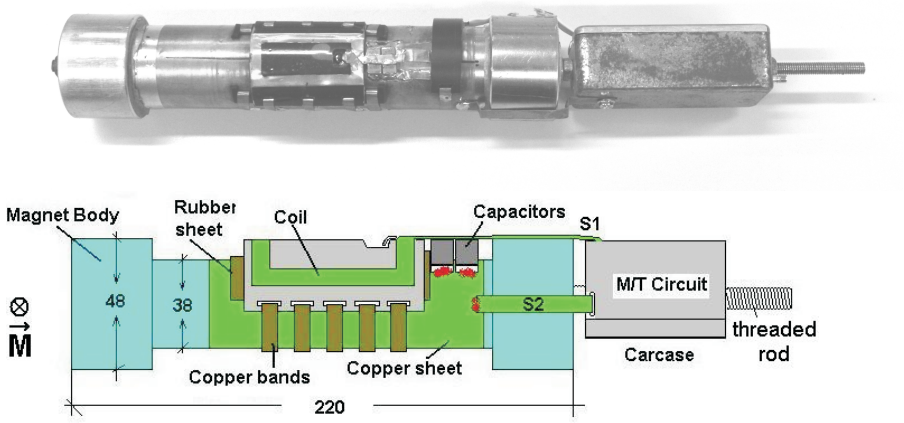

Figure 4.7: Photographed and sketched SLL tool. Units in mm.

As Equation 4.1 suggests, the depth of the sensitive volume, a parameter of key importance to ensure the non-invasive measurement of saturation, influences the actual value of the SNR_{exp} in two ways: By means of the coil

efficiency ω_1/I and also by means of the pulse width t_{180}, which must be readjusted to achieve the 90° tilt of magnetization. Clearly both variables change strongly with the depth, so any change in it induced by a newly set value of the Larmor frequency f_o leads to big differences in SNR_{exp}. Table 4.3, where, together with the readjusted t_{180} at different depths, the values of SNR_{exp} obtained with doped water are presented; illustrates this point clearly: The NMR signal becomes almost ten time weaker when changing the depth from 5 mm to 10 mm, underlining therefore the fact that the depth is a key experimental parameter that determines in a definitive way the final sensitivity of the SLL tool.

Table 4.3: SNR_{exp} of the SLL tool at different depths

Depth (mm)	f_o (MHz)	t_{180} (μsec)	SNR_{exp}
4.7	11.78	10	6.28
6.5	10.6	12	5.4
8.0	9.6	14	2.2
9.6	8.7	29	0.8

In view of these results and bearing in mind that a minimal SNR_{exp} is mandatory to acquire the NMR data with good quality in reasonably time not only with the purpose of measuring saturation but also to acquire a noise-free signal for relaxation analysis, a depth of 4.7 mm (f_o=11.8 MHz) was selected for the experiments performed in laboratory, instead of the 10 mm previously aimed. For *on-field* measurements the depth selected was 8 mm for the experiments (f_o=9.6 MHz), assuring a sensitive volume well incrusted in the natural soil. To further complete this discussion, it is necessary however to explain how the object of measurement, i.e. the partial saturation θ, is obtained through a NMR signal.

4.3.1 Measurement of partial saturation

Strictly speaking, the initial amplitude of the signal is only directly proportional to the number of water spins contained in the sensitive volume. Supposing that in soil with previously unknown partial saturation θ a signal with initial amplitude S_{soil} has been acquired, with the signal in pure water S_{water} and the porosity of soil θ_s, the searched saturation θ will be obtained by a simple linear calibration:

$$\theta = \frac{S_{soil} \cdot \theta_s}{S_{water}}$$

Obtaining S_{soil}, though a simple task, requires however convenient processing to increment the certainty of the measurement, which is intrinsically not very high: As it is stated by the Table 4.3, when working at a depth of 4.7 mm the signal is only 6.2 times bigger than the rms level of the thermal noise. Averaging over the first acquired echoes to obtain S_{soil} certainly would improve this ratio, however it is not clear how many of these echoes can be actually included in the average while still avoiding T_2-weighting in the measured saturation. The following discussion gives an answer to this question: The raw signal supplied by the spectrometer consists of a series of amplitudes of NE echoes separated by an echo time τ_E. In particular for a j-echo, each of these amplitudes can be described by the following equation in dependance of the initial amplitude S_{soil}:

$$S\,[\,j] = S_{soil} e^{-(j-1)\tau_E/T_{2,eff}} + n\,[\,j]$$

where $n\,[\,j]$ stays for the noise component over the j-th echo and $T_{2,eff}$ is the effective value of the transversal relaxation. Despite the presence of this decay, it is advantageous to obtain the relative measure of the saturation S_{water} by averaging over the set of NE echoes: By applying a well known formula, we obtain for this average:

$$< S >= \frac{S_{water}}{NE}\left(\frac{e^{\frac{-(NE)\tau_E}{T_2}} - 1}{e^{\frac{-\tau_E}{T_2}} - 1}\right) + < n >_{NE}$$

And as long as $NE\tau_E < 0.3T_{2,eff}$, we can approximate the exponential term to a linear function ($e^{-x} \approx 1 - x$) within an uncertainty of 5%. Easy manipulations will lead to:

$$< S >= S_{water} + < n >_{NE}$$

So it is proven that averaging over the first NE echoes has no further effect on the obtained data than averaging the random noise, i.e. the obtained average will not be T_2-weighted. Furthermore, this averaging over a data obtained from an experiment repeated NS times diminishes the noise level

to that one we *had* by taking S_{soil} as the initial amplitude in a sequence repeated $NE \cdot NS$ times. When acquiring noisy signals, specially from slightly saturated samples, this procedure is of no little advantage.

4.3.2 Capabilities for relaxation analysis

As has been explained in the section 3.5, the decay of the NMR signal can also provide information about soil as a porous medium. This property opens a secondary aspect to exploit with the SLL sensor. To explore its capabilities in this sense, capabilities which should eventually help to investigate the microscopical aspect of the liquid phase in the soil, the sensor was placed in the shielded calibration cell full of water. The complete decaying signal was then acquired with several values of τ_E with the goal of controlling the influence of the diffusion term in the effective decay. The experimental parameters used were:

Parameter values for the experiment in water
f_o=11.78 MHz, NE=2048, NS=1024 t_{180}=10 μs, R_D=3 s.

The result were analyzed with the ILDT tool, yielding the relaxation spectra plotted in the Fig. 4.8(a) over the T_2^{-1} axis. The reason to choose such a representation will be evident in short.

Initially, the interpretation of these results posed a puzzling challenge given the simple nature of the sample studied and the unique value that the gradient possesses within the sensitive volume. There was thus at first sight no clear reason for having recorded signals in which the spins are evidently relaxing with a variety of values for $T_{2,eff}$. Furthermore, an explanation for the depicted broadness in the relaxation spectra was on demand if this sort of analysis was to yield any information about the sample in a eventual deployment of the sensor to research soils. It was later evident that the found features should be originated in the inhomogeneous character of the rf field. As explained previously, the ensemble of spins in the sensitive volume are subjected to a variety of directions in the effective axis of rotation $\widehat{n}_B$ that affects the relaxation in a way expressed by Eq. 3.10. In the mixture of relaxation modes T_1 and T_2, the transverse relaxation will be dominated by

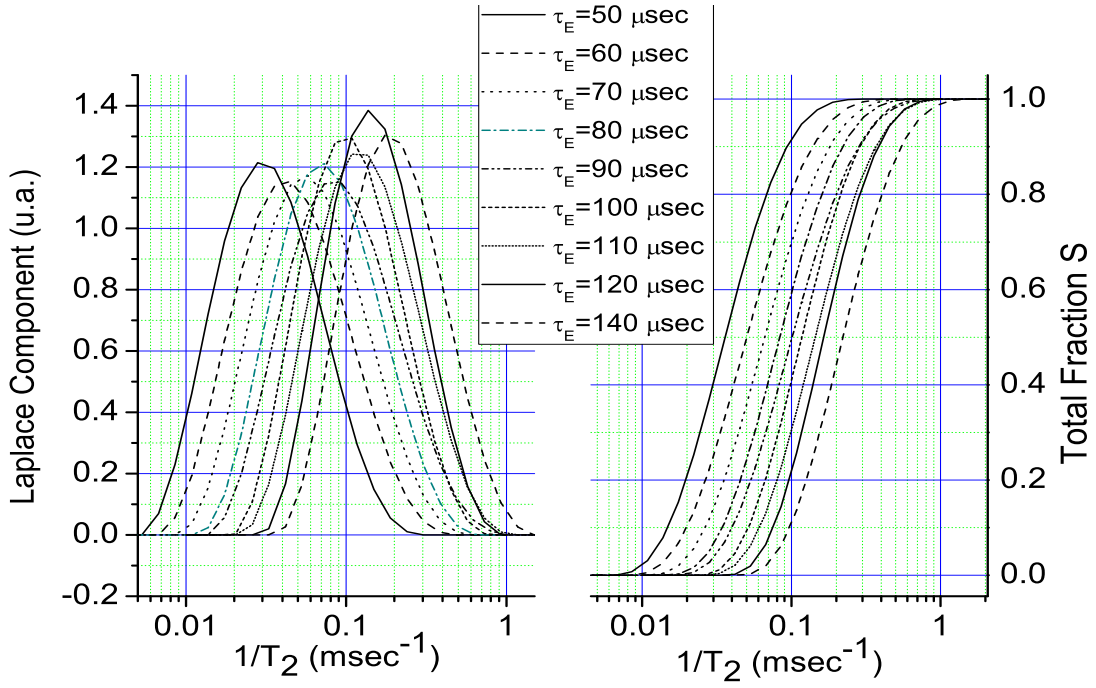

Figure 4.8: (a) Normalized relaxation spectra of Water over T_2^{-1} space acquired with different echo times τ_E. (b) Integrated spectra. S stays for the total fraction of spins.

the diffusion due to the high value of the gradient in this design (22 T/m). Under this condition, an expression for the transverse decay time $T_{2,d}$, that includes the the diffusion effect and neglects pure T_2, term, can be obtained from eq. 3.5 and has the following form:

$$\frac{1}{T_{2,d}} = \frac{Dg^2\gamma^2\tau_E^2}{12}.$$

By replacing this expression into the eq. 3.10 and neglecting the T_1 term due also to the dominance of the diffusion term, the effective transverse decay time $T_{2,eff}$ for an spin with z-component of the local axis of rotation n_z can be obtained:

$$\frac{1}{T_{2,eff}} = \frac{Dg^2\gamma^2\tau_E^2}{12}(1 - \langle n_z^2 \rangle) \tag{4.3}$$

Since $T_{2,eff}^{-1}$ is the quantity against which the relaxation spectra is plotted in the Fig. 4.8, the last equation can be used to reconstruct the dependence between the direction of the effective axis of rotation and the total fraction S of spins in the sensitive volume. Using a more convenient variable to

depict such dependance, the Equation 4.3 is solved for the component of $\widehat{n}_B$ orthogonal to the z-axis: $\langle n_\perp^2 \rangle$=1 − $\langle n_z^2 \rangle$:

$$\langle n_\perp^2 \rangle(S) = \frac{12 \cdot T_{2,eff}^{-1}(S)}{Dg^2\gamma^2\tau_E^2} \tag{4.4}$$

This last equation expresses implicitly the fact that the sought dependance goes through the function $T_{2,eff}^{-1}(S)$. This last function can actually be calculated by the integration of the normalized relaxation spectra of the Fig 4.8(a), an operation expressed in the following way:

$$S\left(t^{-1}, \tau_E\right) = \int_{0.001}^{t^{-1}} f\left(T_2^{-1}, \tau_E\right) dT_2^{-1}$$

and that yields as a result the data plotted in the fig. 4.8(b). As it can be read from such figure, the function $S(t^{-1}, \tau_E)$ is clearly invertible. The inverse function $t^{-1}(S, \tau_E)$ can be calculated by interpolation. When doing so, the relation between $n_\perp$ and the total fraction S can be constructed by performing a fit against τ_E of the Eq. 4.3 on inverse function $t^{-1}(S, \tau_E)$ for a given value of S. To illustrate the result of the procedure, the range of the total fraction S was divided into nine equally separated segments, with the fitting made for each value of S. Figure 4.9 shows the results.

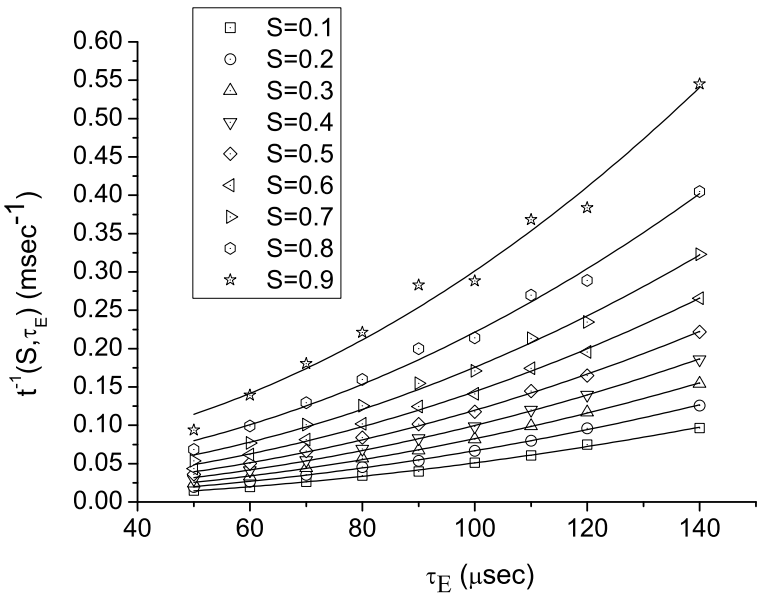

Figure 4.9: Interpolated values of $t^{-1}(S, \tau_E)$ vs. the echo time τ_E. Lines represents equation 4.3 fitted for each value of S.

With the obtained data for $t^{-1}(S, \tau_E)$, the function $n_\perp(S)$ was calculated through the eq. 4.4 (D=2.3 x 10^{-9} m^2/sec), producing the results presented in the following graph:

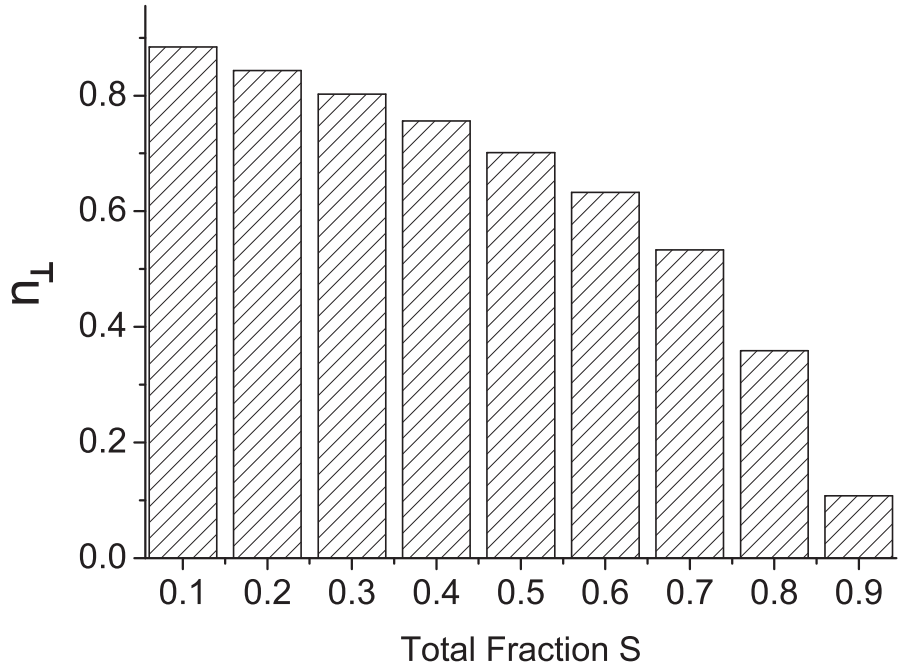

Figure 4.10: Distribution of the projected axis of rotation $< n_\perp >$ against the fraction of spin population in the sensitive volume of the SLL tool. f_o=11.78 MHz, g=23.3 T/m.

Giving this variety of values for the effective axis of rotation, it is clear then that the planar coil, when sending the rf pulses, does not affect all the spins within the sensitive volume equally. The magnetization is tilted differently at different points, depending on how near or far it is from the conductive paths of the coil. Since this effect complicates the interpretation of the relaxation spectra in relation to the study of a generic porous medium, further development of the sensor should take into consideration this fact. In this sense, a coil designed in such a way that all the spin lying in the shell-like sensitive volume that surrounds the magnet are equally excited should be the next natural step to do.

Another aspect tackled during the construction of the sensor was related to the reduction of the external noise. In laboratory experiments, the shielding against external noise was always an important aspect to take care of. Ways to diminish the influence of noise were always searched and researched.

In the envisioned on-field deployment of the SLL sensor, only a partial shielding in the borehole is possible, so approaches to reduce the influence of noise from far-field sources were also researched. Some results in this sense can be reported for the closure of this chapter.

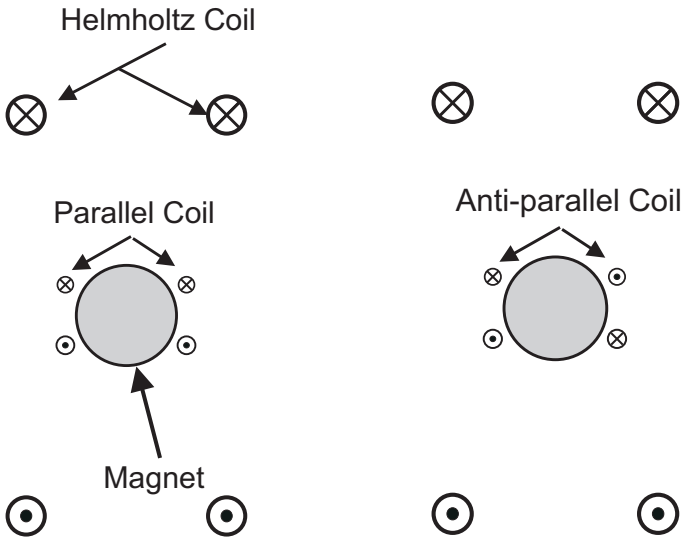

Figure 4.11: (a)Arrangement of parallel planar coils. (b)Arrangement of antiparallel (Gradiometer) planar coils.

A gradiometer coil arrangement, i.e. a pair of planar coils connected in series of antiparallel orientation that theoretically is insensitive to incident planar waves [Sui1], was constructed and implemented in a rf tank circuit tuned at 11.78 MHz. Another arrangement of the same dimension but with the parallel orientation in its constituting pair of coils was also constructed for comparison purposes. To check the insensitivity to far field, they were mounted in the central area of a Helmholtz coil, occupying in both cases a volume where the field lines possess a spatial inhomogeneity lower than 5% [Egh1] in the way despicted in the Fig. 4.11. The Helmholtz coil was made part of an rf tank circuit, also tuned at 11.78 MHz. Results of this test, showed that the antiparallel pair of coils receives the signal form the Helmholtz coil attenuated in 8 dB (in power) in comparison to the parallel pair. Despite this promising results, a circumstance made the actual implementation of this coil in the sensor impossible: Both arrangements exhibited a large magneto-acoustical ringing, perhaps due the their size or the way they were fastened on the body of magnets. The test, however, sets precedence

for future versions of the sensor.

4.4 Conclusions

So far, design considerations about the two conceptions of the low-field NMR instrument for soil research has been presented: The NMR-SPADE and the slim-line logging tool. In the first conception, a numerical calculation of the sensitivity SNR_{theo} for several depths was presented, taking into account the optimized static field at each depth and the amplitude of rf pulses produced by a coil of enlarged dimensions. Due to its low sensitivity at the expected depth, this design was discarded.

In the second conception, a cylindrical sensor called the SLL tool was designed with the goal of, as in the past case, having an uniform value of gradient throughout the expected sensitive volume. This tool was actually built and tested with different f_o, leading to different SNR_{exp} and depths. The cylindrical geometry was the one elected thanks to its adequacy for performing profiles studies of the soil saturation, gaining so information of more interest about its hydrology character.

With the aim of exploring the capabilities of the SLL tool to provide information about the sample beyond the simple measurement of saturation, the complete decaying NMR was acquired with a CPMG pulse sequence and analyzed with the ILD transformation. It was shown that the broad T_2-spectra obtained is associated to inhomogeneities in the effective axis of rotation within the sensitive volume of the tool. When deployed to study soil, the sensor will therefore produce a signal, which once analyzed, must be interpreted with care: The $n_\perp$ inhomogeneity and surface effects will intermingle in the effective relaxation. Although it might be argued that this circumstance complicates the interpretation of the spectra, it is still possible to extract information about the sample exclusively, as the following chapter shows.

Chapter 5

Experiments in Transport of Moisture

5.1 Introduction

Once the SLL tool shows a SNR_{exp} sufficiently high to perform the *ex-situ* measurement, it was deployed to monitor the dynamics of the saturation in model soils. A laboratory setup was built to achieve this goal. Results of the laboratory experiment established the path to follow eventually in the on-field application with the long term objectives of developing a technique to monitor the evolution of the saturation θ and relating this evolution to external variables to which the soil, as physical system, is exposed. In the case of the laboratory experiment, hydrological analysis of the so obtained data will have as objective the determination of the two main hydraulic features of soil: The functions $h(\theta)$ and $K(\theta)$ for the soil, defined already in section 2.1.

Further information about the microscopical conditions of water in the model soils obtained through relaxation analysis of the NMR signal is also presented at the end of this chapter.

5.2 Drainage Experiments

In hydrology, the classical experimental method for the characterization of soils is based on the Klute apparatus [Klu1]. Though its reliability, this method involves a long time of execution, since the measurement are made point to point at hydraulic *equilibrium*. Driven by the need of shortening this time, experiments has been implemented in the *transient* regime of flow, requiring due to their own nature processing of the obtained data. Kool et

al. [Koo1] have shown that the cumulative outflow during time in this regime can be analyzed to obtain the hydraulic properties of the soil, so as they are described by the VGM model (eq. 2.5 and 2.2). Furthermore, Zachmann et. al. [Zac1] also showed that not only the cumulative flow but a time series of directly measured variables like matric head $h(t_k)$ and saturation $\theta(t_k)$ provide enough information to execute algorithms of analysis on this data that supply the sought functions $h(\theta)$ and $K(\theta)$.

In this work, it is shown that this determination from an outflow dataset is possible with a set of variables of a sole type (saturation θ) in two model soils (FH31 and FH31/W3), having this saturation measured via NMR. The model soils studied were: FH31 (coarse sand 100%) and FH31/W3, a mixture of FH31 and fine sand W3 (sand 95%, silt 4%, clay 1%, [Sch4]) in a mass ratio of 1:0.16. Both soils were supplied by the company Quartzwerke in Frechen, Germany. Average surface-to-volume (S/V) ratio for the liquid phase at complete saturation for FH31 was 1/234 μm^{-1} and for FH31/W3 1/108 μm^{-1}, calculated with a Weibull function [Wei1] fitted on the grain size distribution for each sample. Their corresponding setups will make up the so-called FH31 and FH31/W3 experiments.

5.2.1 Experimental conditions

In order to illustrate the evolution of saturation in the transient regime the One-Step Outflow experiment (OSO) was implemented. It was carried out in a column of soil described in Fig. 5.1, composed by an external and an internal tubes of 10 and 5 cm diameter and made of acetate and PVC, respectively. The space between them is filled with the model soil to study, initially saturated with water. At the bottom both tubes are joined to a plastic base that possesses several holes to let water flow. Over the base lies a sheet of filter paper, necessary to permit the movement of water while supporting the soil thereupon.

The whole setup is immersed in a tank which can be filled or emptied with water in less than one minute. Surrounding the tanks stays an iron structure 2.4 m heigh to which a stepper motor is attached that facilitates the movement of the SLL tool along the internal tube. So when the tool acquires at a certain point the NMR signal of the water in the soil, it is lifted to the next point and so completing the profile of the saturation. Since

the stepper motor is connected to the gradient outputs of the spectrometer, the tasks of acquisition and the movement can be controlled from the same spectrometer program. After the simple data processing explained in Section 4.3, a profile of saturation $\theta(z)$, can be constructed along the column depth z.

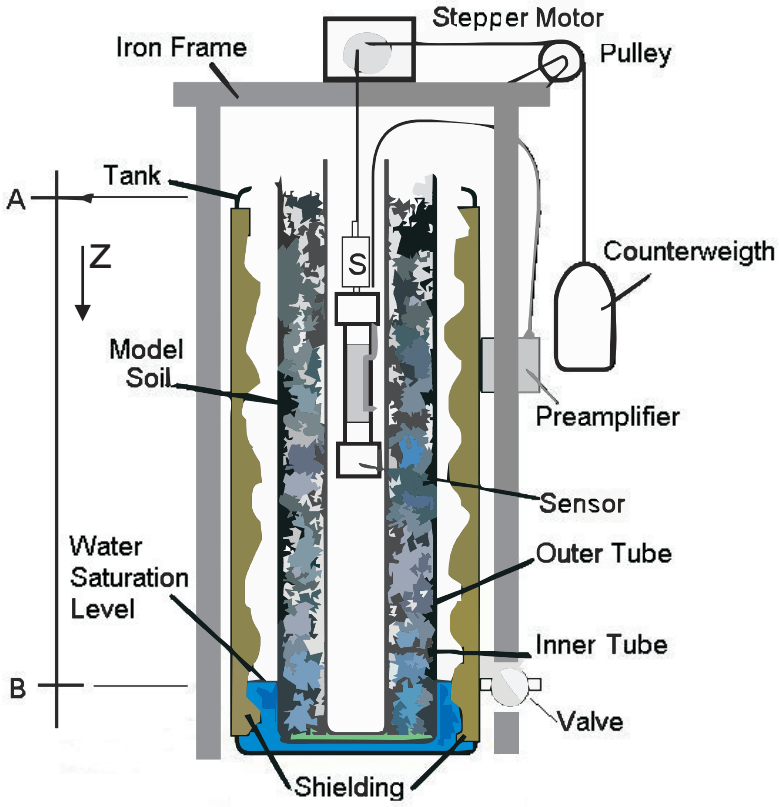

Figure 5.1: Experimental setup for the One-Step Outflow experiment. The height $\overline{AB}$ (180 cm. for FH31/W3 experiment, 70 cm for FH31) goes from the top of the soil (origin of the z axis) to the water saturation level. The valve lets the water to flow out of the tank, initiating the outflow in the column.

Development of the OSO experiment comprises monitoring θ before, during and after the gravity-driven drainage of the column. That requires, in order to set clear conditions that can be corresponded to those considered in the theoretical model, an uniform total saturation of the column of soil as an initial state. While preparing the setup, care must be taken to achieve such an state: When pouring saturated soil into the column, the water saturation level in the tank must be raised accordingly, in order to keep an hydraulic head h around 0 at the top of the soil while it rises. That guarantees uniform

saturation along the column and avoids the soil to be exposed to boundary forces which eventually can separate grains of different sizes, creating crusting and inhomogeneities in the model soil. Since the column is to be treated as a homogeneous hydraulic object, this unwished effect must be prevented to confer reproducibility to experiment.

A crucial requirement for measuring saturation successfully is a robust shielding against all external noise. A conductive parachute silk (shielding in the Fig. 5.1) is wound around the external tube for this purporse. As a rule of the thumb, only when the noise acquired nears the thermal noise level can the shielding be regarded to be good enough to undertake a measurement. In our case this corresponds to a voltage level of 9 nV, calculated using the well known Nyquist formula (Appendix A).

The development of OSO experiments follows three stages:

- **Initial state**: Total saturation of the column. Here a profile of saturation is measured to certify the uniform saturation of the column. The water level in the tank stays at the top level of the soil (Point A, Fig. 5.1).

- **Evolution**. Water is let to flow out of the tank. Meanwhile the sensor is measuring at a certain column depth z_M. The depletion of saturation along time is monitored, producing a time series $\theta(t_k)$. During this depletion, the water saturation level is kept constant at B.

- **Final state**: The column reaches hydraulic equilibrium. A final profile of the saturation is made.

Three curves are therefore obtained: Initial and final profiles (dependent on the column depth) and the evolution curve (dependant on time), which contain enough experimental information to characterize hydraulically the column. As each model soil demanded different effective heights of the soil in the column $\overline{AB}$, measurement depths Z_M and timespan for the evolution stage, these are summarized in Table 5.1, together with gravimetrically measured porosity θ_s for each sample.

Table 5.1: Experimental conditions of the OSO experiments for the model soils FH31 and FH31/W3

	$\overline{AB}$ (cm)	$z_M(cm)$	θ_S	timespan (min)
FH31	60.6	-18.5	0.36	255
FH31/W3(1)	175.5	-14.2	0.29	392

5.2.2 Results

The initial and final profiles for both soils are presented in the Figures 5.2 and 5.3 from NMR data acquired with the following sequence parameters:

Parameter values for the FH31 and FH31/W3 experiment

f_o=11.8 MHz, NE=128, NS=64
τ_E=70 μs, t_{180}=10 μs
R_D=1.5 s (FH31/W3), 3 s (FH31)

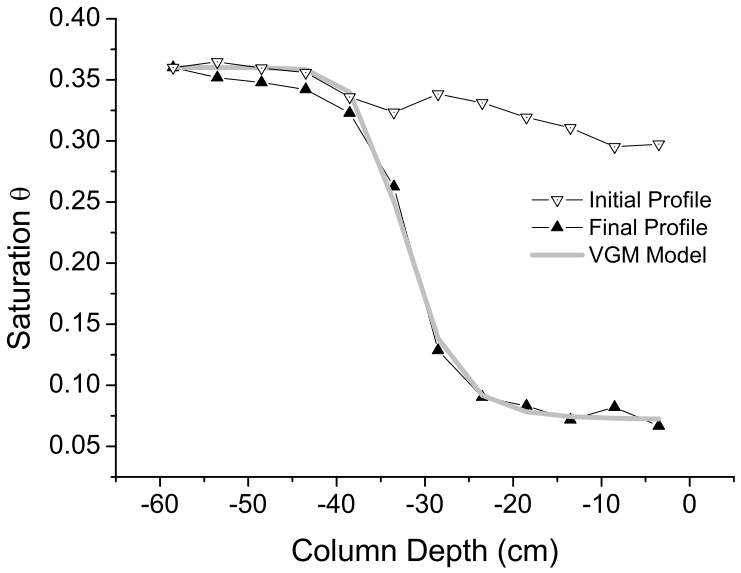

Figure 5.2: Profile of the soil FH31 before and after drainage.

At this stage it is pertinent to make some comments about the quantitative nature of the results prior to their formal hydraulic analysis. As expected for FH31 (Fig. 5.2), the initial profile shows an uniform saturation. In the case of model soil FH31/W3 (Fig. 5.3), although complete saturation is almost achieved, the initial profile shows some irregularities that go

beyond the experimental uncertainty of 6%. A possible explanation for this effect can be the hard-to-avoid crusting that arose while filling the column: The transparent column permitted to observe the accumulation of finer grain at certain positions while being filled. This circumstance however, does not represent a problem in the current hydraulic treatment of the column, as the simulation result will confirm.

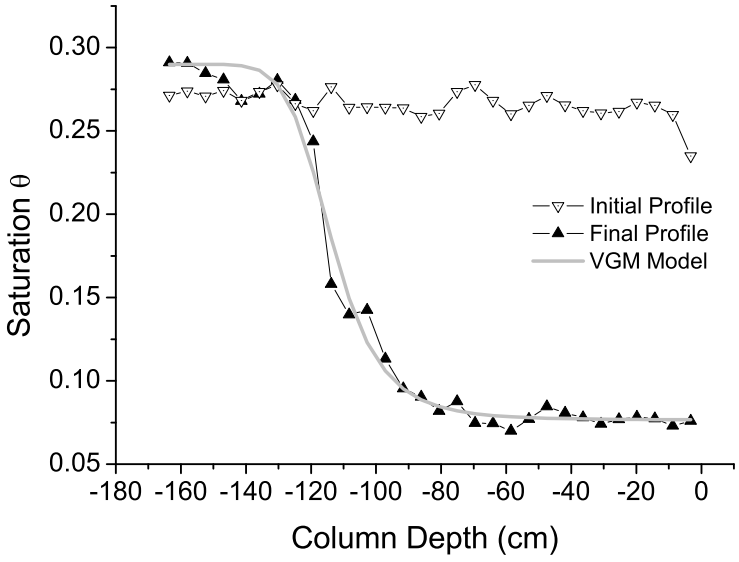

Figure 5.3: Profile of the mixed soil FH31/W3 before and after drainage.

The final profiles in both model soils also already shed some light on their hydraulic features. The profile for FH31 (Fig. 5.2), a mark of the reached hydraulic equilibrium, shows an inflection point at column depth of -30 cm (Height 30.6 cm, measured from the water saturation level) and for the FH31/W3 (Fig. 5.3) at -110 cm (Height 53.5 vm). As discussed previously, the shape in the final profile in height can be taken as a fingerprint of the counteracting effect that the capillary and gravity forces have on the retained water. The difference of about 13 cm in their inflection points can therefore be explained as it follows: The pores in FH31/W3, that has a lower porosity and smaller S/V ratio, exert stronger capillary forces on the absorbed water, making possible its retention at higher positions above the water saturation level in comparison to those in FH31. This fact also underlines the convenience of mixing materials of different hydraulic parameters (as FH31 and W3 are) to compose a model soil of wished hydraulic charac-

teristics: Were W3 alone the soil sample to be studied, the inflection point would lie at a height of 5 m, making the experiment impractical with the available resources. An easy calculation of the inflection point based on the Eq. 2.2 and the hydraulic parameters of W3 [Sch4] proves this point.

Figures 5.4 and 5.5 show the temporal evolution curve during the outflow for both soils. The depletion of saturation in both cases at the corresponding measurement depth Z_M is in each experiment evident.

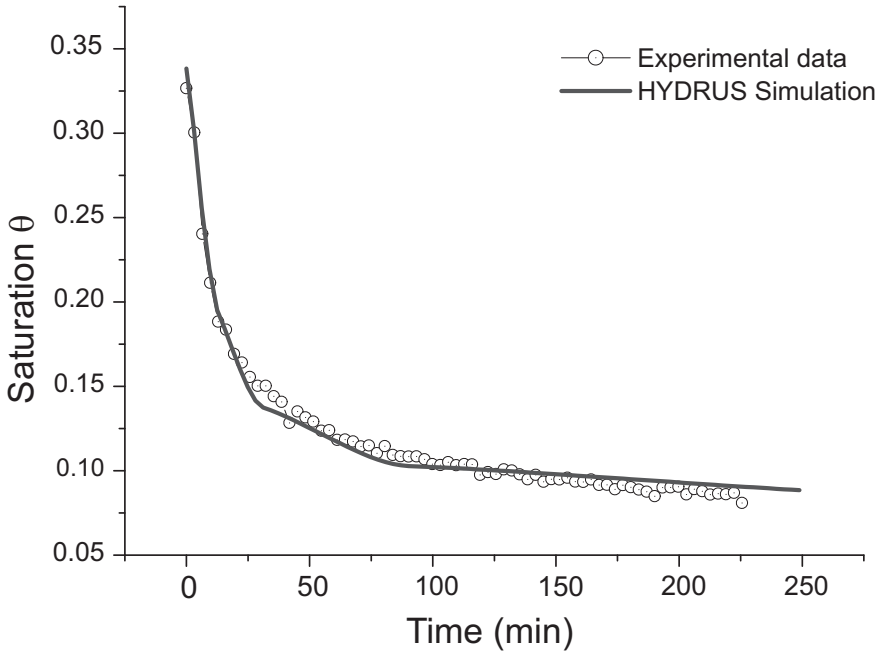

Figure 5.4: Temporal evolution of saturation during outflow in a OSO experiment in soil FH31. Depth of measurement Z_M= -18.7 cm.

5.2.3 Inverse analysis

As pointed out in section 2.1, a complete hydraulic characterization of the model soil means to obtain the values of the VGM parameters: α, n, K_o, l and the residual saturation θ_r, based on the experimental data. Basically there are two curves to model: the final profile, which corresponds to the retention curve $h(\theta)$ and is to be fitted with Equations 2.2 and 2.5; and the evolution curve, fitted with the numerical solution of Equation 2.4. The first part is straightforward and represents no difficulty as the well fitted curve in the fig. 5.2 and 5.3 suggests, being the parameters α and n and the residual saturation θ_r directly obtained.

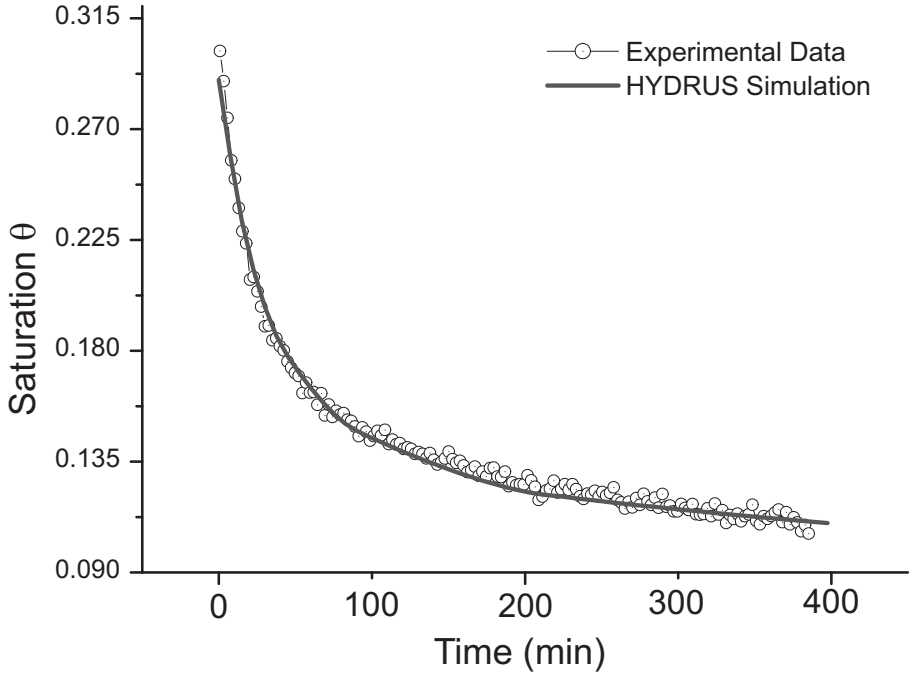

Figure 5.5: Temporal evolution of saturation during outflow in a OSO experiment in soil FH31/W3. Depth of measurement Z_M= -14.2 cm.

The second part, though not that simple, is also straightforward once the numerical tools for its execution are built. It entails the deduction of the remaining parameters K_o (hydraulic conductivity at total saturation) and l (tortuosity factor) through the comparison between the experimental data during outflow and the numerical solution of the Equation 2.4. In this sense, it must be mentioned that the variability in the parameters K_o and l is still a matter of discussion. Although Mualem [Mua1] has shown that a value of 0.5 for parameter l is favored by statistical evidence to construct a comprehensive functional representation of $K(\theta)$, some other authors [Rus1, Sch1] have suggested to take it as an additional fitting factor in the analysis of outflow data. In this dissertation, this last approach is the one assumed. So, over a variety of values for K_s and l, a family of solutions of the Richard Equation are obtained from the HYDRUS 1D program [Šim1], taking as the boundary and initial conditions those defined in the OSO experiment: Constant saturation at the bottom of the column, no flux at the top and soil totally saturated as initial state. By taking different values for K_s and l, a space of solutions is built which is later compared to the time dependant evolution data $\theta_{exp}(t_k)$ through an objective function $\chi(K_o, l)$ defined as:

$$\chi^2(K_o, l) = \sum_{n}^{k=1} \frac{(\theta_{num}(Z_M, t_k, K_o, l) - \theta_{exp}(t_k))^2}{\sigma^2} \tag{5.1}$$

where σ corresponds to the uncertainty of the experimental data θ_{exp}. The minimum of χ over the space (K_s,l) marks the solution θ_{num} that best reproduces the experimental data. This task proceeds with a specially developed MATLAB code[1]. In the determination of the minima the uncertainty σ, though known (6% for the applied sequence parameters), plays no role since all the variables composing the objective function χ are of a sole type. However it is related to the *value* of the minimum, which is always above zero no matter how refined the model may be. Figures 5.6(a) and (b) present the result of these evaluations. Clearly a minimum appears is both cases. The respective solutions are plotted in Figures 5.4 and 5.5 with smooth lines, showing a clear match with the experimental data (circles).

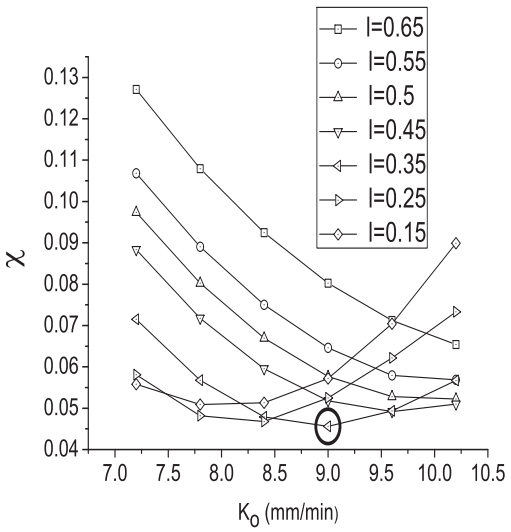

Figure 5.6: (a)Objective function χ for the soil FH31. K_o stays for the hydraulic conductivity at total saturation and l for the tortuosity factor. The minima in both figures are marked by a circle.

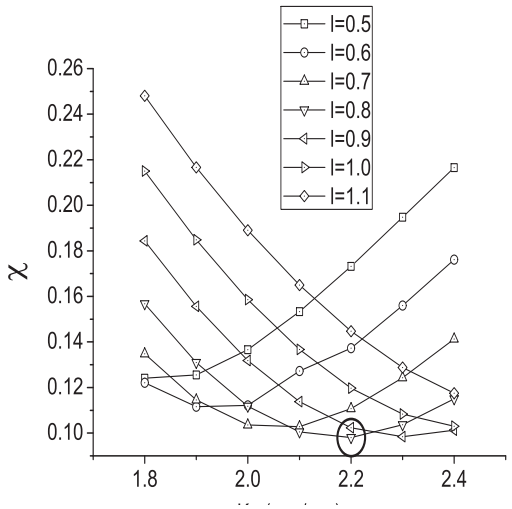

(b)Objective function χ for the soil FH31/W3

Although generally speaking, there can be plenty of minima depending on the character of the experiment performed, in the case of the OSO experiment this minimum happens to be unique thanks the dynamic simplicity of

[1]Developed together with the A. Minière as part of his duties as a research assistant

the problem considered. In more complex situations like multi-step outflows or on-field experiments, that would not certainly be the case. As a matter of fact, this way to estimate of hydraulic properties or, as it is labelled in soil hydrology, *inverse analysis* is currently a flourishing research field, thanks to the improvement of experimental techniques in hydrology and the inexpensive computational tools nowadays available [Hop1].

The obtained VGM parameters for both model soil are presented in the table 5.2.

Table 5.2: VGM parameters for FH31 and FH31/W3 soils

	θ_r	α (/cm)	n	K_s (mm/min)	l
FH31	0.072	0.0357	10.5	9.0	0.35
FH31/W3(1)	0.076	0.0198	7.3	0.035	0.8

Under the consideration of Table 2.1, both soils can be regarded as pure sand. However, a certain difference can be marked from the obtained values. Given the physical interpretation of the VGM parameters (section 2.1), it can be expected that the FH31/W3 possesses a smaller value for n due to its preparation as a mixture. Since the phases which compose it are quite different in their average grain size, it will exhibit a broader distribution of intergrain sizes. Differences in the permeability at total saturation K_s are also expected, due to the difference in the S/V ratio for both soils.

As explained in section 2.1, the factor l expresses at first order how intricate the flow paths are and is less determined by the average inter-grain space. Figure 5.7(a), where the modelled relative permeability $K(\theta)/K_s$ of both model soils using eq. 2.2 is represented against the relative saturation S_e, comes to be of help in this sense. Plotting the relative permeability instead of the absolute permeability assures that the comparison meant is independent on the average dimension of the intergrain space <r>: A necessary condition to draw any conclusion about a shape-governed parameter like l. The graph includes also the relative permeability for W3 phase only, based on data obtained through a multistep outflow experiment [Sch4]. Under these circumstances can these curves be taken as characteristic of the connectivity in the inter-grain space for these model soils.

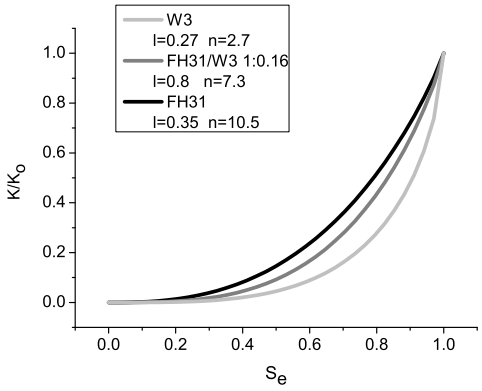

Figure 5.7: (a)Theoretical relative permeability against the relative saturation for FH31, FH31/W3 and W3. Data for W3 taken from [Sch4]

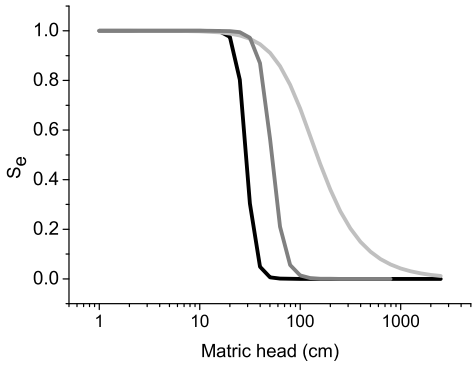

(b)Retention curves for FH31, FH31/W3 and W3.

As it can be seen, is the mixed soil FH31/W3 the one that shows the highest value for the tortuosity factor l of the three model soils, pointing to more tortuous geometry in the flow paths . A reason for this can lie on the fact that although this soil is 84% made of grains of diameter bigger than 250 μm, given the mixture ratio, the small grains of the W3 phase (between 13 and 1 μm) fill neatly the space between the larger grains, complicating thus the geometry of the flow paths. This fact can also explain why the porosity in the soil is slightly lower than for FH31 and W3 phases alone, so as it reads in Table 5.1.

Figure 5.7(b) presents also the retention curves for the three model soils, underlining again the averaging character the mixture soil depicts between the two phase W3 and FH31.

5.2.4 Infiltration Experiment

After having demonstrated that the low-field NMR technique can investigate the hydraulic character of a soil under simple dynamic conditions, additional experiments aimed to reflect more realistic situation like those found in an on-field measurement were implemented. Again making use of the column for the FH31/W3 experiment, this infiltration experiment reproduces a short precipitation event by adding 34 mm of water at the top of the column, being the column at hydraulical equilibrium in its initial state (t=0 min). Due to

its lower permeability, model soil FH31/W3 is convenient for this experience as the evolution of the saturation happens at such a pace that it can be followed by the profiling made with the SLL tool. From this moment on, several profiles of saturation were done sequentially, with results depicted again in Fig. 5.8.

Parameter values for the Infiltration experiment

f_o=11.9 MHz, NE=128, NS=128
τ_E=70 μs, t_{180}=10 μs
R_D=1 s (FH31/W3), Steps: 28)

Given these parameters, each profile demands, including the returning movement of the sensor, 116 min was the time to be complete an experiment.

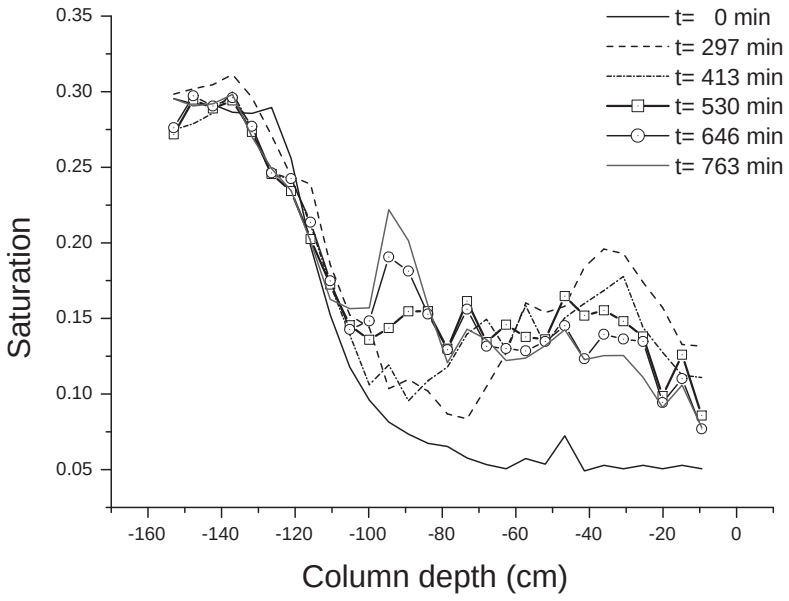

Figure 5.8: Moisture evolution in a column filled with FH31/W3(2) soil, after addition of 34 mm of water. Times t mark the beginning of each profile.

It is important to consider these curves in the context in which they are produced. Given the time the acquisition of each profile demands with respect to the time of evolution, these curves cannot be regarded as an instantaneous picture of the saturation profile. However an evolution can be

appreciated in the Fig. 5.8 that suggest a downwards migration of the infiltration front along time. A local increment of saturation in column depth of -30 cm at t=297 min seems to spread later until it accumulates again at column depth -90 cm at time t=763 min. Water surprisingly does not fall beyond this point, although a few centimeters thereunder the saturation increases again. An explanation for this effect might be that water, as it falls, displaces air that must move upwards through a connected network of empty spaces. However, over a certain of saturation this network percolates no longer, inhibiting therefore the displacement of air. Hence air at depth 100 cm stays trapped, acting as an obstacle for water to further move. In this situation, and specially during the arrival of the infiltration front, pressure gradients in the air phase arise, leading the coupling between the water and air flows, so as it was explained in Fig. 2.1. Modelling of this phenomenon obviously goes beyond the Richard equation and should include a threshold saturation θ_t over which the dynamic regime changes abruptly. Although the development of such a model would lie beyond the scope of the work, it is evident that the low field NMR technique can provide data that pave the way for further developments in the dynamics of fluids in partially saturated porous media.

5.3 Relaxation analysis in partially saturated soils

So far, the tool has been able to perform measurement of partial saturation in a REV. This is however not the sole aspect NMR can explore in the retained water: As explained in Section 3.5, the pace at which the signal decays contains information about the the microscopical environment under which the on-resonance spins are lying. The goal of the experiment performed in this section is then to register how the depletion of saturation influences the relaxation of the NMR signal, opening therefore an opportunity to discern what mechanism of loss of coherence may gain or loss importance as the saturation decreases. After having studied the dynamics of saturation with the OSO experiments, profiles of the saturation in the soil columns in hydraulic equilibrium were made once again, this time recording the complete decaying signal and using the following sequence parameters:

Parameter values for the relaxation experiment in FH31 and FH31/W3

f_o=11.78 MHz, NE=8192, NS=3000
τ_E: 60 (FH31), 70 μs (FH31/W3), t_{180}=10 μs
R_D=3 (FH31), 1.5 c (FH31/W3)

The relaxation spectra for both model soils are plotted in the T_2^{-1} axis, so it has been done Section 4.3. For the FH31, the T_2^{-1}-spectra calculated from the application of the ILD transformation on the NMR data acquired at different column depths are presented in the Fig. 5.9.

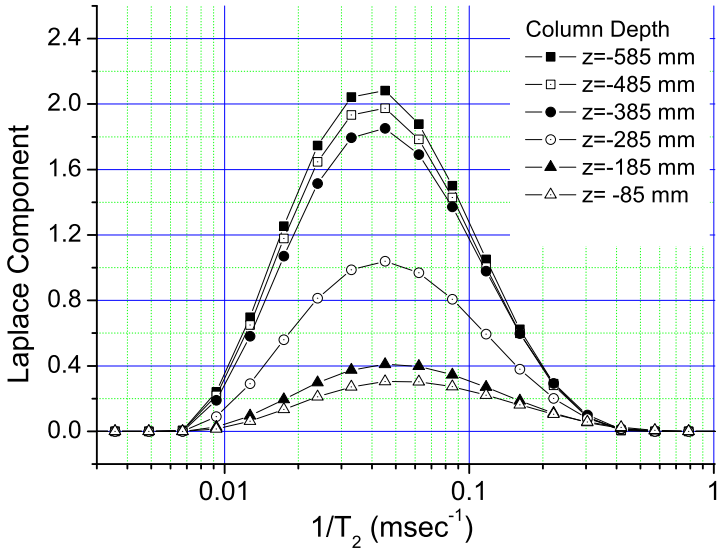

Figure 5.9: Relaxation spectra in the T_2^{-1} space at different column depths for model soil FH31. Black line states for the average T_2^{-1} in water. τ_E=60 μsec.

A first visible feature of the spectra in this figure is their instrument-induced broadness, so as it has been explained in Section 4.3. In spite of this effect, it is still possible to extract information related to the sample exclusively, by using the slight drift observed towards larger values of reciprocal time T_2^{-1} as the saturation diminishes. This drift is manifestation of a relaxation taking place at a faster pace. A convenient variable for the quantitative description of this drift is the average of the spectra $\langle T_2^{-1} \rangle$. This quantity, related to the surface relaxation and the diffusion relaxation through the

eq. 3.13, would take after averaging that equation over a REV the following form:

$$\langle\frac{1}{T_2}\rangle = \rho\langle\frac{S}{V}\rangle + \frac{D\langle\left(\mathbf{g}_o + \mathbf{g}_{surf}\right)^2 n_\perp^2\rangle\tau_E^2\gamma^2}{12} \tag{5.2}$$

where the term $\langle\left(\mathbf{g}_o + \mathbf{g}_{surf}\right)^2 n_\perp^2\rangle$ represents the average of the square of the magnitude of total gradient, that results from the addition of the intrinsic gradient of the tool $\mathbf{g}_o$ and the surface gradient $\mathbf{g}_{surf}$, multiplied by the squared value of the transversal component of the local axis of rotation $n_\perp^2$. Such term can be further developed as it follows:

$$\langle\left(\mathbf{g}_o + \mathbf{g}_{surf}\right)^2 n_\perp^2\rangle = \langle\mathbf{g}_o^2 n_\perp^2\rangle + \langle 2\mathbf{g}_o \cdot \mathbf{g}_{surf} n_\perp^2\rangle + \langle\mathbf{g}_o^2 n_\perp^2\rangle$$

Using a basic theorem of analysis, the middle term of the last equation happens to be upper bounded:

$$\langle 2\mathbf{g}_o \cdot \mathbf{g}_{surf} n_\perp^2\rangle \leq \langle 2\mathbf{g}_o \cdot \mathbf{g}_{surf}\rangle\langle n_\perp^2\rangle$$

and as a natural consequence of the random orientation of the pore surface, the term $\langle 2\mathbf{g}_o \cdot \mathbf{g}_{surf}\rangle$ equals 0. Therefore and taking into account that $\mathbf{g}_o^2$ is constant within the sensitive volume, Equation 5.2 takes the form:

$$\langle\frac{1}{T_2}\rangle = \rho\langle\frac{S}{V}\rangle + \frac{D\langle\left(g_o^2 + \mathbf{g}_{surf}^2\right) n_\perp^2\rangle\tau_E^2\gamma^2}{12} \tag{5.3}$$

To insolate the effect of the porous matrix on the relaxation, it is convenient to recall the results which were obtained when measuring water, presented in the figure 4.8. In that figure, several spectra are plotted, each of them calculated from decays recorded with different echo times. In fact, one of them possesses the same τ_E as the one applied in this experiment (60 μs). Thanks to the same arguments exposed above, the average of such an spectra $\langle 1/T_{2,W}\rangle$ would obeys the following relation:

$$\langle\frac{1}{T_{2,W}}\rangle = \frac{D g_o^2\langle n_\perp^2\rangle\tau_E^2\gamma^2}{12}$$

By subtracting this last equation from the Equation 5.3, this following result appears:

$$\langle\frac{1}{T_{2,Sample}}\rangle = \rho\langle\frac{S}{V}\rangle(\theta) + \frac{D(\theta)\tau_E^2\gamma^2\langle\mathbf{g_{surf}}^2 n_\perp^2\rangle}{12} \tag{5.4}$$

expressing therefore the composed effect of the solid matrix on the relaxation, labelled by the term $\langle 1/T_{2,Sample} \rangle$. The dependencies of the average surface-to-volume ratio $\langle \frac{S}{V} \rangle$ and the diffusion coefficient D on the saturation θ have been introduced explicitly to underline the fact that two are the mechanism through which the depletion of saturation affects the relaxation: Through the surface relaxation, enhancing the pace at which the signal decay, and through the diffusion relaxation. It is important however, in order to picture the frame in which the equation 5.4 is valid, to comment one fact implicitly assumed in this derivation: The diffusion coefficient D has been taken to be equal in both the expression for $\langle 1/T_{2,W} \rangle$ and in the eq. 5.3. Although this holds true when the soil is completely saturated, it is not necessarily the case when the saturation approaches the residual value θ_r. In model soil FH31 for example, the diffusion length l_d of 9 μm ($\sqrt{6D < T_2 >}$) during the sequence is fairly smaller than the average inter-grain space ($< r >$=3/(S/V)≈78 μm). Thus the pore *in average* does not limit the diffusion movement of the spin, a circumstance that makes the considered assumption valid.

In the Figure 5.10 the average of $1/T_2$ for FH31 has been plotted against saturation, based on the data from the Fig. 5.2.

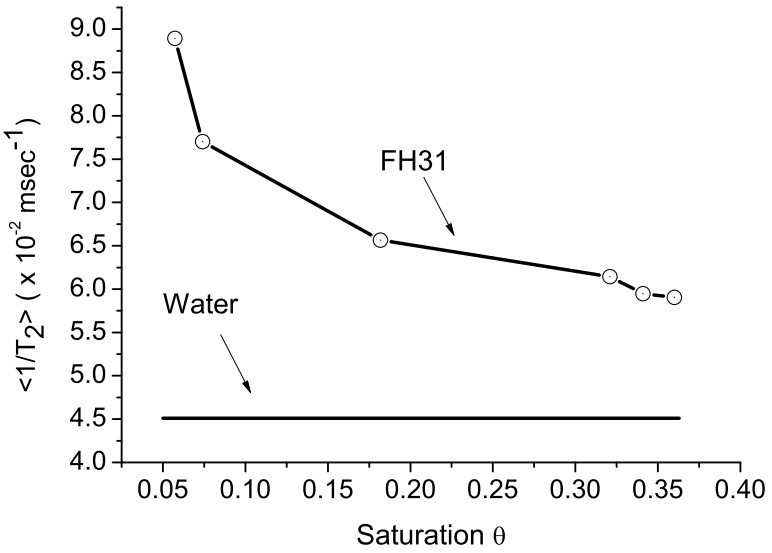

Figure 5.10: (b)Average $\langle 1/T_{2,eff} \rangle$ vs. Saturation θ for model soil FH31. Black line states for the average T_2^{-1} in water. Porosity θ_s=0.36.

For the purpose of guidance, a black line representing the average $\langle T_{2,W}^{-1} \rangle$=(22 ms)$^{-1}$, calculated for the spectra of water acquired with τ_E=60 μs is also despicted in this figure. The difference in height between this line and the actual values of the curve represents thus the quantity $\langle 1/T_{2,Sample} \rangle$, showing a form that is characteristic of the process of losing saturation in the partially saturated soil . This result also proves that, despite of the effect that the multiplicity in the effective axis of rotation $n_\perp$ has on relaxation, the SLL sensor do supply data which, conveniently processed, is of help in forming a picture of what is happening to the liquid phase as the saturation decreases.

The situation for the model soil FH31/W3 is, although similar, not equal. In Fig. 5.11 the corresponding relaxation spectra are presented, acquired

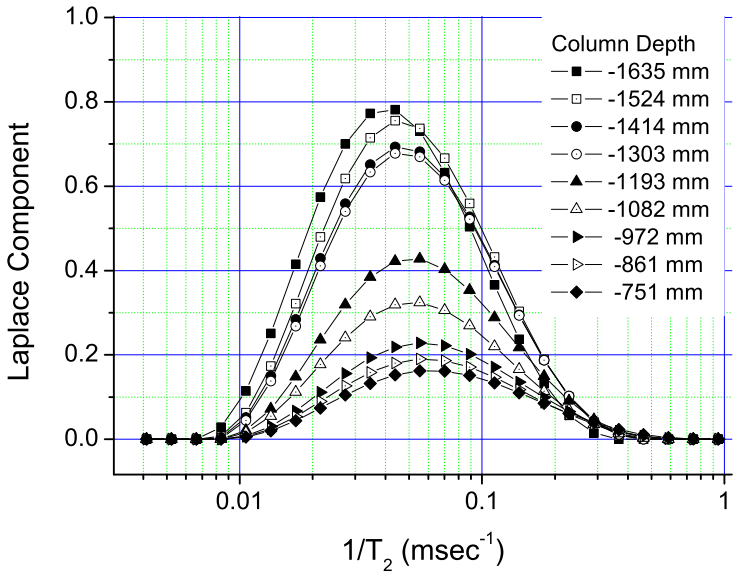

Figure 5.11: Relaxation spectra in the T_2^{-1} space at different column depths for model soil FH31/W3. Black line states for the average T_2^{-1} in water. τ_E=70 μsec.

In a similar way, calculation of the average $1/T_2$ against saturation, also making use of data from Fig. 5.3, produced the result of Fig. 5.12. Here also the black lines stays for the average $T_{2,W}^{-1}$ for water ((17 ms)$^{-1}$, τ_E=70 μs). The diffusion length l_d, practically with the same value than in the previous experiment, is still smaller than the average pore size $< r >$ of 36 μm for model soil FH31/W3. These are however of the same magnitude in this case.

Therefore, it is to expect that a sizable fraction of the total on-resonance spins do bound against the pore walls during the timespan of pulse sequence, causing a change in the diffusion coefficient D. Thus, the equality of the diffusion term for $\langle 1/T_{2,W} \rangle$ and the eq. 5.3 can not be assumed in the case of model soil FH31/W3 anymore. Furthermore, the fact that the difference in height between the black line and the curve for the Fig. 5.12 is not always positive can be seen as a consequence of this abrupt change in the character of the diffusion.

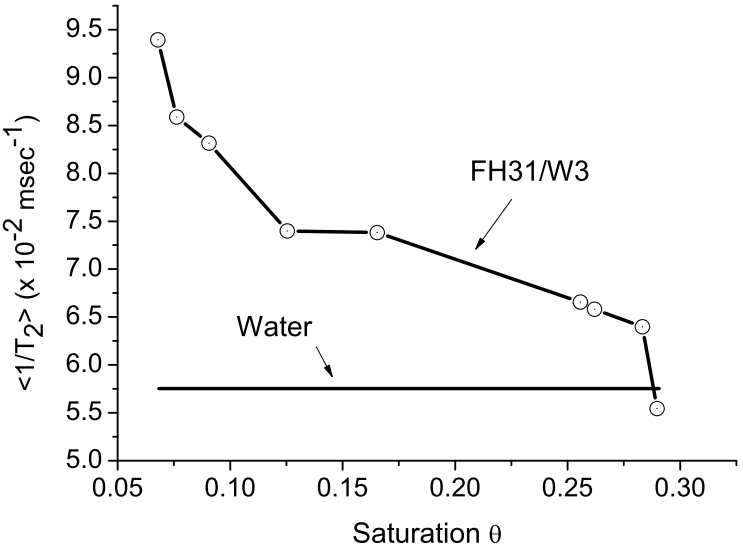

Figure 5.12: (b) Average T_2^{-1} vs. saturation for model soil FH31/W3. Black line states for the average T_2^{-1} in water. Porosity θ_s=0.28.

Finally, an important detail must be mentioned: Due to the additive character each relaxation mechanisms exhibit in the T_2^{-1} space, averaging the spectra over this space means also averaging over the distribution of S/V ratio any porous media possess, specially when it is partially saturated. The obtained quantity is therefore a more adequate one for purpose of comparison than $\langle T_{2,eff} \rangle$ or the maxima of the spectra, as the last discussion has assumed.

5.4 Conclusions

It has been shown that the tool is successful in supplying saturation data with a resolution in time and uncertainty low enough to monitor the water

flow in model soils in uncoupled (OSO experiments) and coupled regimes (infiltration experiment). The supplied data can also be inverse analyzed to obtain the VGM parameters of the soil under research.

Posteriorly, it has been seen that the tool not only measures partial saturation θ but also can provide, through ILD transformation, information about the relaxation processes taking place in the retained water. Although in its current state, the so obtained relaxation spectra have a shape that is strongly determined by the field characteristics of tool, they can be further analyzed under certain assumptions to discern the way the proper model soil influences them. Several are the mechanisms through which influence takes place and the challenge of disentangling them should certainly be taken as incentive for future developments of the tool.

Chapter 6

Field Measurements

As mentioned in the introduction, a long-term goal of the research project in which this dissertation is framed is the successful implementation of low field NMR as technique to measure soil moisture *on-field* [TR32, 2010]. To demonstrate this possibility, the setup of the OSO experiment was installed in the lower part of the TRANSREGIO test site, located in Selhausen near Düren, Germany. The site belongs to the basin of the Rur river. The major soil type is silt loam according to the USDA textural classification [Wei2].

Outdoor implementation of this experiment requires careful evaluation of each aspect involved, specially those related to noise reduction. The NMR technique is very sensitive to electromagnetic noise, which must therefore be assessed well before undertaking any measurement of saturation: Usually the voltage induced in the rf coil by the spins on resonance is very small (order of nV, see appendix A) and barely higher than the thermal noise unavoidably present. For this reason the measurement entails tackling difficult issues which in the laboratory are not given, as the exposition to far-field noise in the outdoor case is higher. New approaches to reduce EM noise must always be tried. Among them was the construction of the gradiometer coil, a test already described in the past chapter. Though this criticality, the encouraging fact that the movement of the sensor had been automatized made feasible the outdoors measurement, under the assumption that the final influence of noise in the results can always be reduced with a sufficiently high number of scans NS.

Perforation of the earth to make space for the SLL tool was naturally the first step to make. For this task, three steel tubes, of different lengths

(70, 120 and 170 cm) and same external diameter (5 cm) were deployed. In each of them, the internal edge at one extreme was sharpened until it shows a knife-like blade. At the other extreme, a hole was drilled perpendicular to the axis 5 cm thereunder. With the tubes ready and waiting for a day in which the soil is sufficiently humid, the smallest one is first rammed into the earth with a teflon-made hammer. Once the tube is completely completely buried, an aluminium pole, going through the hole previously drilled, serves to draw out the tube. Later is introduced the consecutively larger tube, and the operation is repeated. A hole 170 cm deep in the earth was made in this way, exhibiting a clean internal surface thanks to the cutting effect of the blade.

Posteriorly a PVC tube, where the sensor will move and of the same kind used in the laboratory set up, was introduced in the borehole. A half circle of this tube is covered with an electrically grounded cooper foil, which is kept attached by a fabric tape. While being introduced, the orientation of the tube must also take into account the geographic north, so it is shown in the Fig. 6.1. So, the tool, which while being hauled behaves as a compass due the magnetic field of earth, always faces the foil-free side of the tube. Using this approach the noise level (rms) could be reduced from 200 to 50 nV, when thermal noise was measured to be 27 nV.

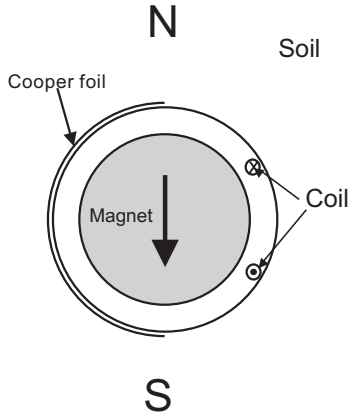

Figure 6.1: Tube orientation. N are S represent the geographical poles.

Over the borehole, naturally, stays the iron structure that permits the automatized profiling. An small angled roof was constructed over the stepper motor to make the structure weatherproofed. A tent with the spectrometer and the computer was set 2 meters away from the structure as the Fig. 6.2 shows. In the Figure 6.3 the area around the borehole is zoomed, showing

Figure 6.2: Set up for the *on-field* measurement of saturation. The tent contains the measurement electronics.

the tool while being introduced.

The experimental parameters used were:

Parameter Values for the *on-field* experiment
f_o=9.94 MHz, NE=256, NS=1024, Steps=26 τ_E=70 μs, t_{180}=14 μs, R_D=1.5 s.

and the results for the dates September 23^{rd}, 25^{th}, 26^{th}, 27^{th} and 29^{th} 2010 are presented in figure 6.4.

Calculation of the experimental uncertainty proceeded so: As explained in section 4.3.1, only the echoes that lie above the 75% of the initial value must be included in the averaging for the calculation of the partial saturation. Since such a way of averaging assumes a linear approximation for the decay, the uncertainty of each saturation point, represented in Figure 6.4 by the error bars, was taken as the standard deviation of the difference between the actual value of the echoes and the best fitted straight line for the averaged decay.

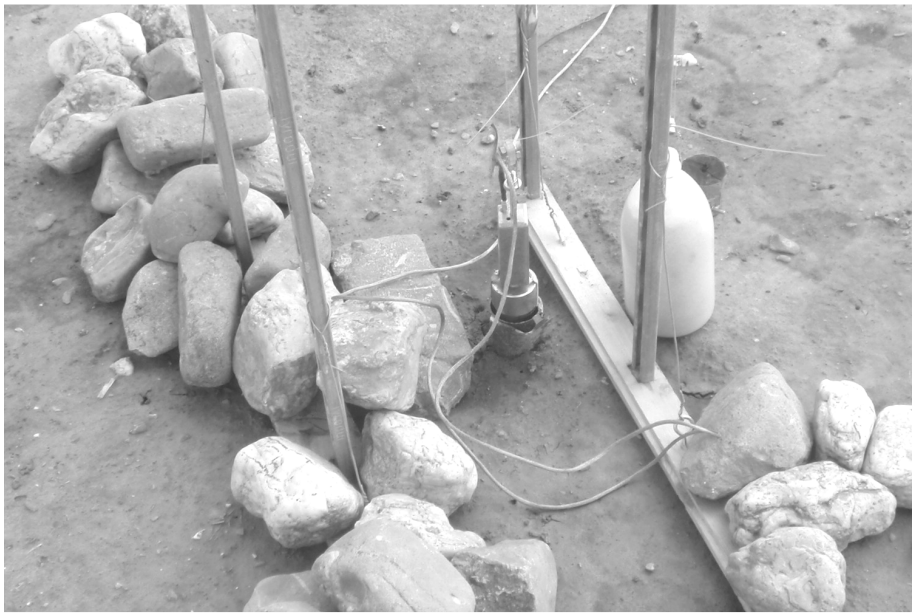

Figure 6.3: The SLL tool being introduced in the borehole.

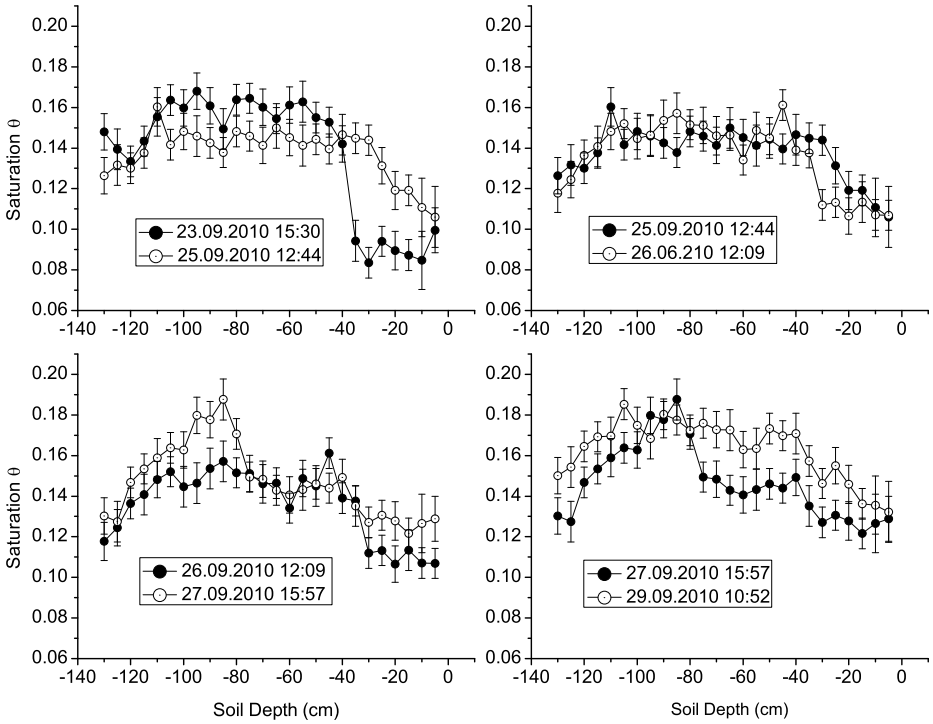

Figure 6.4: Results of the measurement campaign. Each graph present the profiles of two consecutive measurements. Maximum depth: 120 cm.

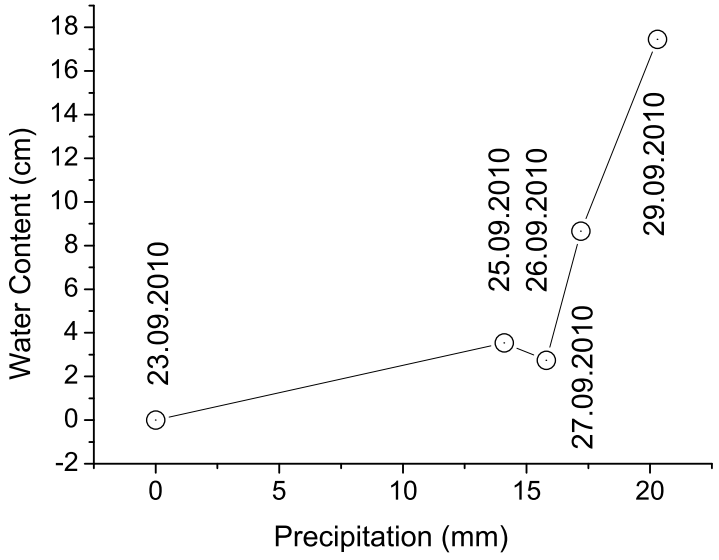

Figure 6.5: Integrated profiles vs. Precipitation.

The Figure 6.4 contains also the saturation profiles in sets of consecutive measurements in order to make the contrast between profiles more visible. An evolution from day to day can be appreciated, and without aiming to construct a quantitative explanation of the obtained data in the way done in the section 5.2, some considerations can be made over this data which reinforce the scientific value of this technique in concerns of *on-field* hydraulic analysis of soils.

Undoubtedly, the general evolution of the saturation is determined in natural conditions by a set of external factors like precipitation, evaporation, drainage and the proper hydraulic nature of the soil under research. The influence of main climatological variables on this evolution, the precipitation, can in fact be established with the available data. Precipitation data from a drop counter installed in the site helps to explore this influence, as the graph 6.5 shows: In this graph, water content per area is calculated by integration of the profiles of Fig. 6.4. The differentials in water content in the measured range (with respect to the first day of measurement) are plotted against the accumulated precipitation.

Two conclusions can be drawn from the graph 6.5: First, as the data in the ordinate almost monotonously increases with time, an overall increment

in the saturation for the Selhausen soil is the first feature of the observed evolution. Secondly, a partial correlation between water content and precipitation is found. Therefore, it can be said the precipitation during these 8 days is directly related to the observed increment in soil moisture.

Figures 6.4 and 6.5 confer validity to the data acquired with the SLL tool to monitor effectively saturation. A total correlation cannot, naturally, be expected, as variables like the water drain, evaporation and the proper hydraulic character of the soil have not been taken into account. It is however clear that improvements in the technique and the inclusion of these mentioned variables can provide eventually data prone to be inverse analyzed. The obtention of the hydraulic parameters of the soil from such *on-field* data, measured in a non-invasive way with NMR, would be certainly a great contribution in the development of experimental techniques in soil hydrology.

Chapter 7

Conclusions and Outlook

The task of designing and constructing a low-field NMR tool specially tailored for on-field measurement of soil saturation has been brought forward with this dissertation. Some scientific achievement made in this sense were

7.1 Conclusions

1. **Prediction of the sensitivity for a generic MOUSE-based NMR sensor**. Taking advantage of the field features the static field in the NMR-MOUSE has, a analytical expression for the expected Signal-to-Noise Ratio (SNR_{theo}) was derived. It was seen, that given a sensitive volume of certain field magnitude B_o and gradient g, the next most important factor that determines the sensitivity is the pulse width t_{180} and effective excited area A at a depth y_o. The formula predicts quantitatively the experimental sensitivity of the MOUSE and represents a refinement to a previous calculation made by Perlo [Per4].

2. **Design of the NMR-SPADE**. The static field of several magnet design was solved and the expected saturation calculated. Due to the low sensitivity obtained for the constrained depth (0.8), the approach with the NMR-SPADE was discarded.

3. **Design and construction of the SLL tool**. Assuming a dumbbell-like geometry for the body of magnet, a cylindrical tool was designed under the constraint of having a constant gradient in a sensitive volume with a depth of 10 mm. The tool was in fact constructed, partially due to the reason that it better suits to perform profiling in soils so in the same way as the well logging tools. Its performance at different

depths was studied, and its capability to measure partial saturation was tested. It was also found through relaxation analysis that the coil exerts its tilting effect on the magnetization with different efficiencies within the sensitive volume.

4. **Drainage experiments in model soils**. After having construction a setup that permits the complete saturation of a soil-filled column, the gravity-driven drainage of the retained water was followed in two kind of model soils, FH31 and the mixture FH31/W3.

5. **Inverse Analysis of the OSO experiment**. Based on the dynamical evolution of this drainage, the hydraulic parameters of the model soils have been deduced using methods of inverse analysis. This experiment proves, with known boundary condition of the system, the capability the SLL tool has to supply data useful for a hydraulic characterization of soil.

6. **Relaxation Analysis of NMR data**. Through the application of the ILDT transformation on NMR data acquired with a CPMG sequence in both partially saturated model soils (columns in the hydraulic equilibrium), several relaxation spectra or distribution in the space of T_2^{-1} were produced at different partial saturations. Though entirely considered, the effects from the field features of the tool and from the model soil on the spectra are intermingled, it was possible to make an assessment of the composed effect that the partial saturation has on the relaxation.

7. **Field measurement of saturation**. Using an automatized profiling, it was possible to perform measurement of saturation up to 1.2 mt in depth in the TRANSREGIO test site in Selhausen near Düren, Germany. The importance of reducing external noise with conveniently deployed shielding was established. The profiles made during a one-week long measurement campaign reflect the overall increment of saturation due to 20 mm of rain fallen in that week.

Finally, and in regard to the operational aspect of the developed tool, the advantage of having a non-invasive way of measuring partial saturation should not be overseen. Boundary effects that might arise when the usual experimental techniques like TDR and tensiometers are badly coupled to the

soil under research are not of concern with the presented tool.

7.2 Outlook

Trying to resume the presented work in few words, this dissertation describes the first steps toward a reliably and robust low-field tool for outdoor characterization of soil. Several aspects can be mentioned which make the tool worthy of further development, since it can open a flourishing field in the pillars this dissertation is grounded on, namely the NMR instrumentation and experimental techniques of soil hydrology.

The tool in its current state can be deployed in outflow experiments of higher dynamics richness which could put into the test not only the models for the hydraulic characteristics of the soil $\theta(h)$ and $K(\theta)$ but also the algorithms that are applied in inverse analysis. This is an actual topic in research in hydrology nowadays [Hop1].

Furthermore, the composed character expressed by eq. 5.4 of the effect of the sample on the relaxation should be taken as incentive for improvement of the tool. In the middle term, it is wished a tool which can be deployed outdoors and supplies through relaxation analysis information less determined by the instrument features and more by the microscopical conditions of the retained water. This entails basically improving three aspect such as: immunity of the rf coil to far-field noise, improved design of rf coil to correct the variability in the local value of $n_\perp$ and to improve the conversion of the electrical rf power into rf field without detracting the thermal noise figure (adjusment of the quality factor of the tank circuit).

Once these improvements are implemented, it would be possible to use stimulated echoes (instead of Hahn echoes) to separate the contribution of diffusion and surface on the relaxation spectra, so it has been already accomplished for the NMR-MOUSE [Rat1]. Estimation of the microscopical parameters like average S/V and diffusion coefficient in partially saturated soil would be possible, producing a data of firm scientific value for the modelling of these systems and to research their relation to their hydraulic behavior of the soil.

Appendix A

A theoretical Signal-to-Noise Ratio

A.1 Introduction

With the aim of having an estimation of the Signal-to-Noise Ratio (SNR) that could serve in the conception of the NMR SPADE, the calculation of this experimentally defined parameter was undertaken based on theoretical considerations. Although Hoult et al. [Hou1] already present a theoretical treatment of this problem, their work is limited to the case of homogeneous fields. In this sense, some of their premises are assumed in this work for the case of the inhomogeneous field found in the magnet designs like that of the NMR-SPADE.

This so called "theoretical" SNR_{theo} is later compared to an proper experimental SNR_{exp}, measured in each case for two coils of different sizes and at different depths D (Fig. A.2) and using a magnet of dimensions 300 x 300 mm^2, further described by Perlo et al. [Per1]. The temporal parameters of the CPMG sequence, the actual depths used and the dimension of the coil determine also the input data applied in the calculation. From the agreement between these two quantities the validity of the theoretical approach has been attested.

A.2 The experimental signal-to-noise ratio

Experimental conditions for :

- **NMR Parameters**: Frequency f_o=8.2 MHz, pulse length t_{180}=35 μs, echo time τ_E=130 μs, NE=32, NS=8, acquisition window ACQ=40 μs, recycling delay R_D=0.5 sec, gradient g=2.5 T/m, susceptibility of rubber χ_{Rubber}=1.0 * 10^{-9}.

- **Coil Dimensions**: A larger coil, called just BIG of external dimensions 45 x 52 mm^2, and a smaller coil, called just SMALL of dimensions 36 x 44 mm^2. Both coils are made of 4 turns of cooper wire of diameter 1.47 mm.

- **Depth Explored**: The distance between the coil and the sensitive volume D, as shown in Fig. A.1, was swept between 7 and 16 mm in steps of 1 mm. The sample consisted of a rubber cube of dimensions 40 x 40 x 60 mm^3.

It is important, in the wish of conferring coherence to this discussion, to mention the reason of employing coils of two different sizes. Numerical calculations of $\mathbf{B}_1$ using the Biot-Savart law suggested a slight enhancement of 30% in the value of the field at depths larger than 13 mm for the BIG coil in comparison to the values of encountered for the SMALL coil. These coils were therefore constructed to determinate whether such an enhancement in field would actually improve SNR_{exp} at such depths.

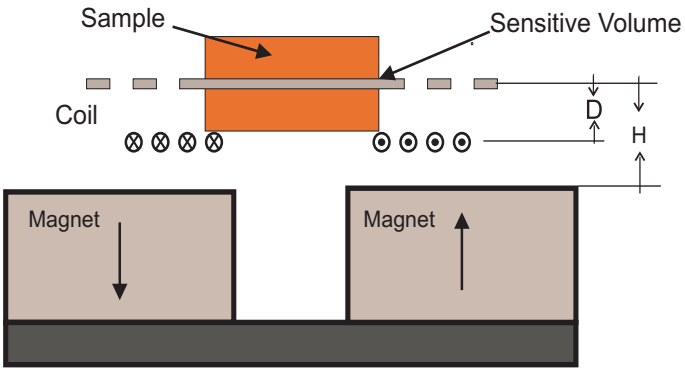

Figure A.1: Setup for the experimental determination of SNR with a NMR-MOUSE.

Figure A.1 makes clear the arrangement for the determination of SNR_{exp}. As mentioned, D is the depth and H is the distance between the sensitive volume and the top of the magnet, which, for a Larmor frequency of 8.2 MHz correspond to 29 mm. So, by varying D while keeping H constant, the

change of SNR_{exp} at each depth can be followed without having to retune the rf tank circuit of the coil. As the definition of SNR_{exp} states (eq. 4.2) which requires beyond the signal S, the sequence parameters NE and NS, and the standard deviation σ. This last quantity was calculated at each depth over a population of 20 measurements.

In order to obtain figures for SNR_{exp} strictly comparable to each other, and under the circumstance that the thickness of the sensitive volume is determined by the finite width of the pulse t_{180}, it is necessary at each depth to readjust the rf power to comply with the refusing condition of the pulse while keeping t_{180} constant. Results of the measurement are depicted in Fig. A.2 for both coils at the mentioned depths, with the error bar corresponding to the standard deviation at each depth.

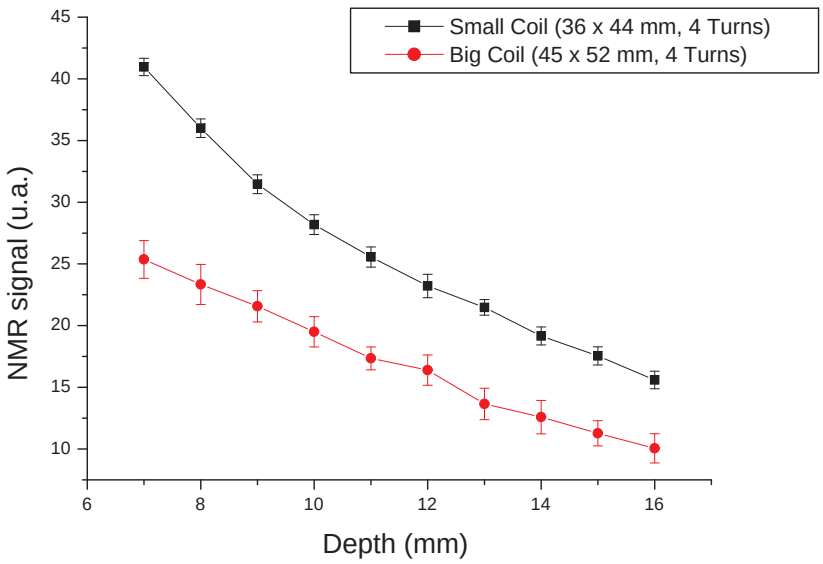

Figure A.2: NMR signal with statistical uncertainties for different depths, measured with the BIG and SMALL coils. Experimental parameters: f_o=8.2 MHz, NE=32, NS=8, τ_E=130 μs, t_{180}=35 μs. Rubber Sample: 40 x 40 mm^2.

One first interesting fact regarding these results was the difference between the signals for the BIG coil and the SMALL coils. The SMALL coil performed considerably better even at depths for which the field in both coils was expected to be the same. This might be originated on the fact that in the SMALL coil, as having smaller quality factor, the current decays faster

after the pulse goes off. In fact, considering the applied sequence parameters, the voltage in the coil must drop from the 300 V immediately after the off-switching to nV level in less than 30 μsec. This gives an idea of how critical the AC characteristic of the coil are for the good performance of a low field NMR instrument, making room to introduce in the future more improvement in this element,

A.3 The theoretical signal-to-noise ratio

Following the definition of SNR_{exp}, a theoretical equivalent can be constructed from the ratio of the induced voltage in coil by the spins on-resonance V_{signal} and the voltage of the thermal noise V_{noise}:

$$SNR_{theo} = \frac{V_{signal}}{V_{noise}}$$

Therefore, to complete the calculation of SNR_{theo} it is then mandatory to execute the calculation of the quantities V_{signal} and V_{noise}.

A.3.1 Calculation of the NMR signal

Although other authors [Bal1, Zur1] have purposed several methods to calculate the NMR signal in low-field applications , we follow the suggestion of Hürlimann and Griffin [Hür1] to calculate the voltage induced in the coil by a population of on-resonance spins distributed over a volume V, expressed by eq. A.1.

$$V_{signal} = \frac{\chi}{\mu_o} \int_V dV \mathbf{B}_o^2(\mathbf{r}) \frac{\omega_1(\mathbf{r})}{I} F\Big(\Delta\omega_o(\mathbf{r})\Big) m_{\infty,y}(\mathbf{r}) \qquad \text{(A.1)}$$

where $\omega_1(\mathbf{r})/I$ is the efficiency of the coil to detect the signal from the on-resonance spins at position $\mathbf{r}$. This last scalar quantity is based on the frequency equivalent of the rf field $\mathbf{B_1}$ defined in the eq. 3.8. $F(\Delta\omega_1)$ stays for the spectral response of the rf tank circuit, which depends directly on the offset frequency $\Delta\omega_o$. Following its definition (eq. 3.7), the sensitive volume V is located in first order at the places where the offset frequency equals 0. Evaluation of Eq. A.1 must occur over this volume V. That is, of course, only possible with a previous knowledge of the spatial dependence of $\mathbf{B}_o$ and $\mathbf{B}_1$. For the static field in the magnet design under consideration, this can be described by the Eq. A.2, where B_o is the magnitude of static field at resonance (0.19 T) and g the value of the gradient (2.5 T/m) in the

case of the permanent magnet used in the experimental determination of the SNR_{exp}.

$$\mathbf{B_o} = B_s\widehat{z} + g \cdot (y - y_o)\,\widehat{z} \tag{A.2}$$

This equation assumes the frame of reference depicted in the Fig. 4.1, where the y_o comes to be the depth of the sensitive volume, measured from the top of the coil. Equation A.2 expresses also a common feature of all magnet design based on the NMR-MOUSE: The uniformity for the gradient of the static field over a large volume, which, for this particular magnet, is maintained for a depth y_o between 19 and 39 mm (25 and 45 mm measured from the top of the magnet, as the coil lies 6 mm over it [Per1]).

The calculation of the reception efficiency ω_1/I for each coil and depth y_o, follows straightforward from the rf field $\mathbf{B_1}$ and on the Equations 3.6 and 3.8.

With the elements that composes the formula A.1 evaluated, the next natural step, i.e. the execution of the integral, is facilitated by the introduction of an approximation that takes advantage of the symmetries presented in the static and rf fields. Bearing this objective on mind, it is pertinent to study the implications the function $m_{\infty,y}$ has on the sensitive volume V.

As the Fig. A.1 suggest, the sensitive volume exhibits a form of almost flat slice of certain thickness Δy thanks to the (at first approximation) the uniformity of the gradient on the plane XZ and with the assumption of conveniently adjusted magnitude of the rf field, $\omega_1{=}\pi/t_{180}$ over the excited slice. Along the Y axis, the effect of spins that continuously win and loose their resonance condition can be easily depicted by plotting $m_{\infty,y}$ over the $\Delta\omega_o$-axis, so as it has been done in the Fig. A.3 (continuous curve). This curve represents an 1D profile of the excited slice and can be seen also as a cut of Fig. 3.3 though the line A. Again in the Fig. A.3, the small peaks, in appearance modulated by a sinc function envelope, are expression also for the coherence enhancements that arise due imperfect rf-pulses or frequency offsets. They actually contribute very little to the final profile, and in fact, play a role in the coherence evolution mostly in its transitional regime [Hür1].

Naturally, it is the peak corresponding to $\Delta\omega_o{=}0$ the one that dominates the conservation of coherence during the sequence. This is not a surprise, of

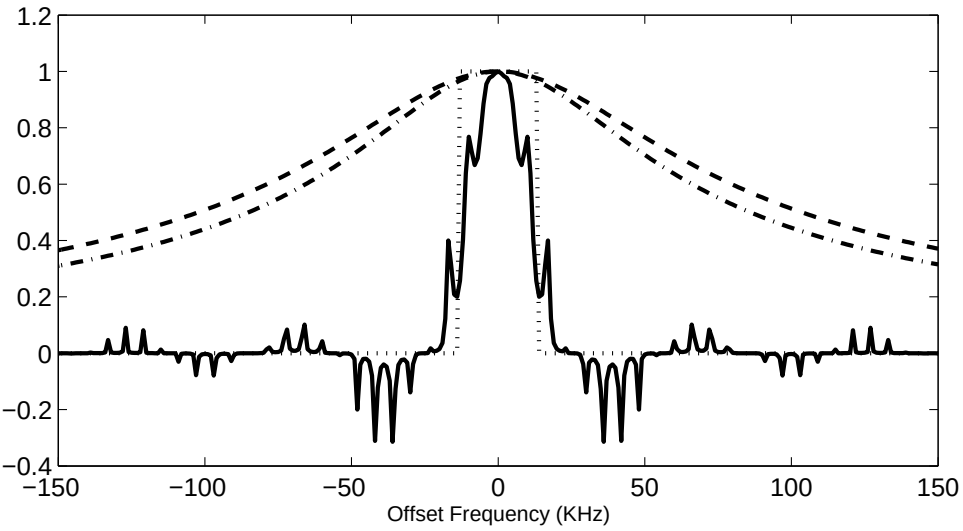

Figure A.3: $m_{\infty,y}$ vs. $\Delta\omega_o$ (solid). ω_1=π/t_{180}, τ_E=130 μsec, t_{180}=35 μsec. Step function ($\delta\omega_o$=25 KHz, dotted). $F\left(\Delta\omega_o\right)$ for the SMALL and BIG coils (dashdot and dashed respectively).

course. However, the utility of Fig. A.3 goes beyond that fact: It shows also that this 1D profile of the sensitive volume or slice, can be approximated by a hat function defined by a width Δy.

The width of the hat function determines thus the thickness of the excited slice. Introducing its definition by taking the middle point between the origin and the first zero from the generic expression of $m_{\infty,y}$, the thickness Δy is given by the Eq. A.3.

$$\Delta z = \frac{\sqrt{3}\pi}{t_{180}\gamma g} \tag{A.3}$$

Using the purposed approximation to replace $m_{\infty,y}$ and the spatial dependence of the static field given by the Eq. A.2, the formula A.1 takes then the form:

$$V_{signal} = \frac{\chi}{\mu_o}\int_{y_o-\Delta y/2}^{y_o+\Delta y/2} dy \int_A dxdz\Big(B_o + g\left(y-y_o\right)\Big)^2 \frac{\omega_1\left(x,z,y\right)}{I} \tag{A.4}$$

As the form of this integral hints, a further approximation on ω_1 can be of advantage, specially after setting the origin of the variable of integration y at the middle of the excited slice $y = y_o$. A Taylor expansion around the depth of the excited slice y_o implements it, as the following equation states:

$$\begin{aligned}\omega_1(x,y,z) &= \omega_1(x,y_o,z) + \frac{\partial\omega_1(x,y_o,z)}{\partial y}(y-y_o) + \\ &\quad \frac{1}{2}\frac{\partial^2\omega_1(x,y_o,z)}{\partial y^2}(y-y_o)^2 + \ldots\end{aligned}$$

The introduction of this series in the Eq. A.4 allows to further develop it. So, a series in powers of the slice thickness Δy is obtained for the V_{signal} around the depth of the sensitive volume y_o. For the first two non-zero terms, such serie S takes then the following form:

$$\begin{aligned}V_{signal} &= \frac{\chi}{\mu_o}\int_A dxdz B_o^2\frac{\omega_1(x,y_o,z)}{I}\Delta y + \\ &\quad \frac{\chi}{\mu_o}\int_A dxdz\frac{1}{12I}\Big\{\frac{B_o^2}{2}\frac{\partial^2\omega_1}{\partial y^2} + 2B_o g\frac{\partial\omega_1}{\partial y} + \omega_1 g^2\Big\}\Delta y^3 + \ \ldots\end{aligned}$$

This last equation is in fact a meaningful one when interpreted under the light of the influences the changes in the rf and the static exert on the final value of V_{signal}. The first term express the fact that once the pulse successfully achieves to tilt the magnetization at the given slice of thickness Δy, it is the integration of coil efficiency ω_1/I over the plane XZ what determines the actual value of the induced NMR signal. This result represents a refinement in comparison with previous calculation made by Perlo [Per4], where the value, without performing any integration, of ω_1/I at the excited slice is the leading term in establishing the sought strength of the NMR signal. There is of course no second order term in the series, due to the even character the step function possess around the middle point of the slice. The third order term is an expression of the influence the local changes of the static and rf fields within the sensitive volume have on the V_{signal}. In the numerical evaluation of this term for the coil geometries and magnet design here considered, it never exceeded a value higher than 3% of that of the first term. It is of sense therefore to neglect it for any further consideration.

By substitution of the slice thickness (Eq. A.3) in the last equation, a first-order approximation for V_{signal} can be so presented:

$$V_{signal} = \frac{\chi}{\mu_o} B_o^2 \int_A dxdz \frac{\omega_1(x, y_o, z)}{I} \frac{\sqrt{3}\pi}{t_{180}\gamma g} \qquad \text{(A.5)}$$

As this last equation states, the following statement can be then taken as the conclusive remark of this section: The integration of the reception efficiency ω_1/I of the coil over an certain area A is enough to calculate the voltage induced by the spins in the coil, multiplying the result by the corresponding terms. Easily it can be also seen that after calculation of the rf field for each depth y_o, the Equation A.5 can be evaluated directly. The task was accomplished either in this appendix and in the section 4.2 with the same MATLAB® code.

With respect to the area A, dependent on the depth y_o, a further detail must still be noted: The area A changes little with the depth, as the fig. A.4 suggests: The contour shows the points for which $m_{\infty,y}$=0.5 at different depths for the BIG coil, with the coil self represented by the regular dashed square. Following the shape of the different contours, it can be seen that the excited slice cast resemblance with the coil at the smallest depths. If the depths increases, this resemblance becomes weaker, although the area enclosed by the contour line (a quarter of A) changes little.

Another aspect that is related to the experimental determination of SNR_{exp} and should not be overseen is the following one: In the range of depths considered (7-16 mm), it is always assumed that the local magnetization is refocused. At longer depths, this entails the delivery of pulses of higher power. The power capabilities of the deployed equipment are of importance in regard to this point. For the case of current consideration, the supplied power of 2000 W of the TECMAG rf amplifier utilized in this work are enough to fulfill this condition only with a t_{180} of 35 μs. Naturally, this is the value to be use in the evaluation of equation A.5.

A.3.2 Thermal noise

Thermal noise, an unavoidable companion in the acquisition of AC signal of very weak amplitude, is originated by the fluctuations in the local density of free electrons due to their thermal movements [Ede1]. A well known formula given by Nyquist describes the root-mean-square level of this noise V_{noise} present in a coil that possess a resistance R_{AC} against a current oscillating

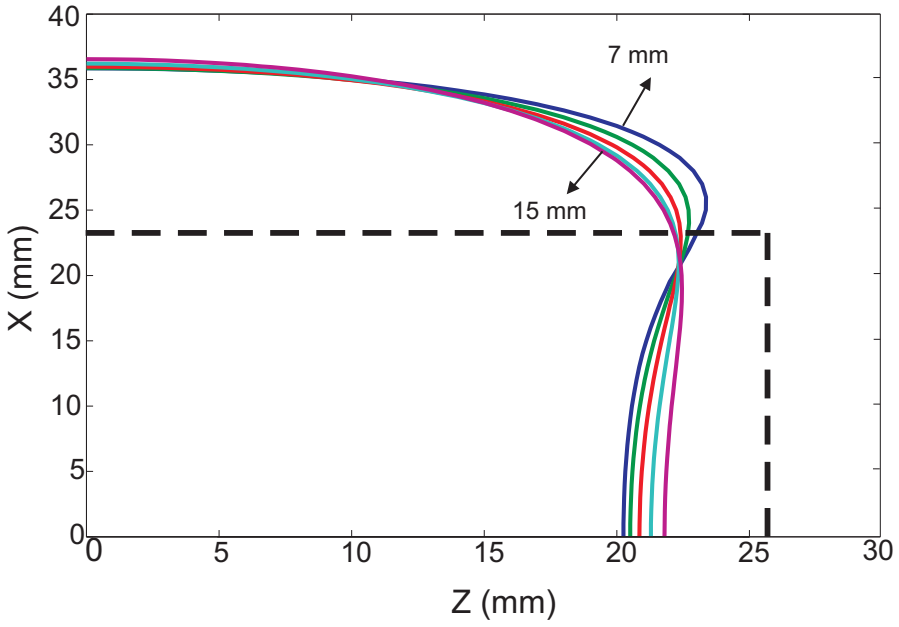

Figure A.4: Contour curves for a asymptotic transverse magnetization $m_{\infty,z} = 0.5$, induced over the XZ plane by the coil BIG. τ_E=130 μsec, t_{180}=35 μsec. Depths: 7, 9, 11, 13 and 15 mm. The dashed line represents the coil BIG.

with frequency f:

$$V_{noise} = \sqrt{4kTR_{AC}\Delta f} \tag{A.6}$$

where T is the absolute temperature of the coil, Δf is the spectral bandwith of the coil, acting as a receiving element, and k the Boltzmann constant. To evaluate this equation it must be reminded that the coil belong to a rf tank circuit which posses important AC features like the resonant frequency f_o and the quality fact Q. For the case of our concern, the calculation of the noise level V_{noise} requires the measurement of the Q for both coils, a task that can be easily accomplished in a spectral analyzer. Δf can be then obtained by using a the *operational* definition of Q=$\Delta f/f_o$. The other variable needed for the evaluation, R_{AC}, demands the measurement of the inductance of the coil L, which can be solved from the *theoretical* definition of Q=$\omega_o L/R_{AC}$. The measurement of L can be done indirectly using the matching and tuning conditions for the rf tank circuit, expressed by the following formulae [Kod1]:

$$R_{eq} = Q\omega_O L \left(\frac{C_t + C_m}{C_t}\right)^2$$

Table A.1: Electrical features and thermal noise for the BIG and SMALL coils.

	Q	L (μHy)	$R_{AC}(\Omega)$	V_{noise} (nV)
Big Coil	83	1.2	0.89	42.0
Small Coil	69	0.7	0.47	27.9

$$\omega_O^2 L\left(C_t + C_m\right) = 1$$

where C_t and C_m are the tuning and matching capacitors of the rf tank circuit, being the first usually the only variable known a priori when tuning the rf tank circuit. R_{eq}, the equivalent resistance of the tank circuit, equals 50 Ω when matched with the standard value of the internal impedance in any rf equipment. Once the matching and tuning conditions are achieved C_t and C_m can be deduced from these last two equations and also so R_{AC}. Evaluation yielded the results presented in the Table A.1:

As a corollary added to this discussion, an advantage of measuring the AC features of the coil lies on the fact that the normalized spectral response $F\left(\Delta\omega_o\right)$ (Eq. A.1) of the rf tank circuit can be firmly determined, using a classical equation for the module of the AC impedance $|Z_p|$ of a parallel connected tank circuit evaluated over the space of the *absolute* frequency ω [Pfe1]:

$$|Z_p| = R_{AC}\sqrt{\frac{\left(Q\omega/\omega_o\right)^2 + 1}{\left(1 - \left(\omega/\omega_O\right)^2\right)^2 + \left(\omega/\omega_O Q\right)^2}}$$

The advantage of the formulation of $F\left(\Delta\omega_o\right)$ becomes evident when examining Fig. A.3, where an unitary $\widehat{F}\left(\Delta\omega_o\right)$ for both coils is also depicted in an axis centered on the operation frequency used (8.2 MHz): The figure allows to consider in comfortable way over the axis of the offset frequency $\Delta\omega_o$ the response of the tank circuit and the excited bandwidth of the sensitive volume. As it is easy to recognize, the frequency responses for the both coils shows a bandwidth quite broader than the excited band of the sensitive volume. This fact makes unnecessary their consideration in the evaluation of the Eq. A.1, as the past development has assumed.

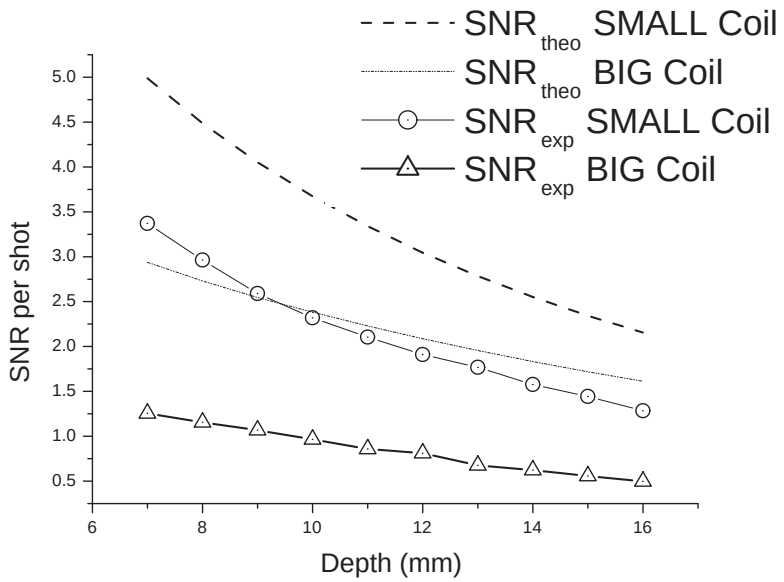

Figure A.5: SNR per shot for the Big and Small Coils. g=2.5 T/m, f_o=8.2 MHz, t_{180}=35 μs. Sample: Rubber, χ=$1.0 * 10^{-9}$.

A.4 Theoretical SNR vs. experimental SNR

Evaluation of Eq. A.5 over the limits given by the rubber sample, and divided by the corresponding V_{noise} produced the theoretical SNR (SNR_{theo}) depicted in Fig. A.5. The experimental SNR are plotted there as well.

Although the prediction does not perfectly match and in fact a systematic difference in the absolute values of about 50% must be addmited, we can take the theoretical values as an upper limit for the SNR under given $\overrightarrow{B_o}$ and $\overrightarrow{B_1}$. This difference, regarded to be a a consequence of the limited capacity the coil possesses to change from the transmission (and conducting currents of several amperes) to the reception modes (receiving voltage at the nV level), can be tolerated for the purpose of the design the eq. A.5 is intended for.

Bibliography

[Anf1] S Anferova, V Anferov, J Arnold, E Talnishnikh, MA Voda, K Kupferschläger, P Blümler, C Clauser and B Blümich. Improved Halbach sensor for NMR scanning of drill cores, *Magn. Reson. Imaging* **25** (2007) 474480.

[Bal1] F Balibanu, H Hailu, R Eymael, D Demco and B Blümich. Nuclear Magnetic Resonance in inhomogeneous fields. *J. Magn. Reson.* **145** (2000) 246-258.

[Bea1] J Bear, Dynamics of Fluids in Porous Media, Dover, New York, 1988.

[Blü1] B Blümich, Essential NMR, Springer, Berlin, 2005.

[Blü2] B Blümich, P Blümler, G Eidmann, A Guthausen, R Haken, U Schmitz, K Saito and G Zimmer. The NMR-MOUSE: Construction, Excitation and Application, *Mag. Res. Imaging.* **16** (1998) 479484.

[Blü3] B Bluṁich, NMR-Bildgebung in den Materialwissenschaften, Nordrhein-Westfälische Akademie der Wissenschaften, Vorträge zur 483. Sitzung, Verlag Ferdinand Schöningh, München, 2004, pp. 3354.

[Bro1] HW Brown Capillary pressure investigations, *Trans. A.I.M.E.* **192** (1951) 67-74 .

[Cas1] F Casanova and B Blümich, Two-dimensional imaging with a singled-sided NMR probe, *J. Magn. Reson.* **163** (2003) 38-45.

[Car1] HY Carr and EM Purcell. Effects of diffusion on free precession in Nuclear Magnetic Resonance Experiments, *Phys. Rev.* **94** (1954) 630-639.

[Coa1] G Coates,L Xiao and M Prammer M. NMR Logging Principles and Applications, Halliburton Energy Services, Houston (1999).

[Dai1] W Daily, A Ramirez, A Binley and D LaBrecque. Electrical resistance tomography theory and practice, in: DK Butler (ed), *Near-Surface Geophysics, Investigations in Geophysics*, 13, Society of Exploration Geophysicists, Tulsa, 2005, pp. 525-550.

[Ede1] F Eder. Moderne Messmethoden der Physik. Teil III. VEB, Berlin, 1972.

[Egh1] IR Eghrari and P Costa Ribeiro. Simple Method for Checking the Balance of Gradiometers Used with SQUIDS, *Rev. Bras. Fis.*. **10** Nr. 1 (1980) 115-119.

[Fol1] I Foley, A Farooqui and R Kleinberg, Effect of Paramagnetic Ions on NMR Relaxation of Fluids at Solid Surfaces, *J. Magn. Resn.* A 143 (1996) 95-104

[Fur1] EP Furlani. Permanent Magnet and Electromechanical Devices. Academic Press, New York, 2002.

[God1] S Godefroy and Callaghan P, Two dimensional relaxation/diffusion correlation in porous media. *Magn. Res. Imaging* **21** (2003) 381-383.

[God2] S Godefroy, JP Korb, M Fleury and RG Bryant, Surface nuclear magnetic relaxation and dynamics of water and oil in macroporous media. *Phys. Rev. E* **64**, 021605.

[Hah1] EL Hahn, Spin echoes, *Phys. Rev.* **80** (1950) 580594.

[Hop1] JW Hopmans and J Šimůnek, Review of inverse estimation of soil hydraulic properties, in: MT van Genuchten, FJ Leij and L Wu (eds.), *Proceedings of the International Workshop on Characterization and Measurement of the Hydraulic Properties of Unsaturated Porous Media*, University of California, Riverside CA, 1999, pp. 643659.

[Hür1] M Hürlimann and D Griffin, Spin Dynamics of Carr-Purcell-Meiboom-Gill-like Sequences in Grossly Inhomogeneous B_o and B_1 Fields and Application to NMR Well Logging, *J. Magn. Resn.* **143** (2000) 120-135.

[Hür2] M Hürlimann and L Venkataramanan, Quantitative Measurement of Two-Dimensional Distribution of Diffusion and Relaxation in Grossly Inhomogeneous Fields, *J. Magn. Reson.* **157** (2002) 31-42.

[Hou1] DI Hoult and RE Richards, The Signal-to-Noise Ratio of the Nuclear Magnetic Resonance Experiment. *J. Magn. Reson.* **24** (1976) 71-85.

[Jac1] JA Jackson, LJ Burnett, F Harmon, Remote (inside-out) NMR. III. Detection of nuclear magnetic resonance in a remotely produced region of homogeneous magnetic field, *J. Magn. Reson.* **41** (1980) 411421.

[Kim1] R Kimmich, NMR Tomography, Diffusometry, Relaxometry, Springer, Berlin, 1997.

[Kle1] RL Kleinberg, Well logging, in: DM Grant and RK Harris (eds), *Encyclopedia of NMR*, Wiley-Liss, New York, 1996, pp. 49604969.

[Kle2] RL Kleinberg, A Sezginer and DD Griffin. Novel NMR Apparatus for Investigating an External Sample. *J. Magn. Resn.* **97** (1992) 466-485.

[Kle3] RL Kleinberg, WE Kenyon and PP Mitra. Mechanism of NMR Relaxation of Fluids in Rock, *J. Magn. Reson.* **A 108** (1994) 206-214 .

[Klu1] A Klute. Laboratory measurement of hydraulic conductivity of unsaturated soil, in: CA Black (ed.) *Methods of Soil Analysis*. Monograph 9. Amer. Soc. Agron., Madison, Wisc, 1965, pp. 253-261

[Kod1] VD Kodibagkar and MS Conradi. Remothe Tuning of NMR Probe Circuits. *J. Magn. Resn.* **144** (2000) 53-57 .

[Koo1] JB Kool, JC Parker, MTh van Genuchten. Determinatining soil hydraulic properties from one-step outflow experiments by parameter estimation: I. Theory and numerical studies. *Soil Sci. Soc. Am. J.* **49** (1987) 1348-1354 .

[Mar1] A Marko, B Wolter and W Arnold, Application of a portable nuclear magnetic resonance surface probe to porous media, *J. Magn. Reson.* **185** (2007) 19-27.

[Mat1] GA Matzkanin, RF Paetzold, Measuring Soil Water Content Using Pulsed Nuclear Magnetic Resonance, *ASAE Winter Mtg.*, Paper No. 82-2619, Chicago, Illinois, 1982.

[Mei1] S Meiboom and D Gill Modified Spin-Echo Method for Measuring Nuclear Relaxation Times. *Rev. Sci. Instrum.* **29** (1958) 688-691 .

[Mej1] M Meju, P Denton P and Fenning. Surface NMR sounding and inversion to detect groundwater in key aquifers in England: comparisons with VESTEM methods. *J. Appl. Geophys.* **50** (2002) 95111.

[Mit1] PP Mitra, PN Sen and LM Schwartz. Short-time behaviour of diffusion coefficients as a geometrical probe of porous media, *Phys. Rev. B* **47** (1993) 8565-8575.

[Mua1] Y Mualem Y. A new model for predicting the hydraulic conductivity of unsaturated porous media. *Water Resour. Res.* **12** (1976) 513-522.

[Oso1] JS Osoka, JG Richarson, JK Kerver, JA Haford and PM Blair PM. Laboratory measurements of relative permeability, *Trans. A.I.M.E* **192** (1951) 47-55.

[Per1] J Perlo, F Casanova and B Blümich. 3D imaging with a single-sided sensor: an open tomograph. *J. Magn. Reson.* **166** (2004) 228235.

[Per2] J Perlo, F Casanova and Blümich B. *J. Mag. Res.* **176** (2005) 6470.

[Per3] J Perlo, F Casanova and B Blümich. Ex Situ NMR in Highly Homogeneous Fields: ^1H Spectroscopy. *Science* **315** (2007) 1110-1112.

[Per4] J Perlo. Single-Sided NMR Tomography. Dissertation. RWTH Aachen (2006).

[Pfe1] H Pfeifer. Elektronik für den Physiker. Verlag Akad. Ver., Berlin ,1967.

[Rat1] DG Rata, F Casanova, J Perlo, DE Demco and B Blümich, Self-diffusion measurement by a mobile single-sided NMR sensor with improved magnetic field gradient, *J. Magn. Reson.* **180** (2006) 229235.

[Rob1] DA Robinson, SB Jones, JM Wraith, J Or and FP Friedman. A Review of Advances in Dielectric and Electrical Conductivity Measurement in Soils Using Time Domain Reflectometry. *Vadose Zone J.* **2** (2003) 444475.

[Rot1] K Roth. Soil Physics. Lecture Notes. Institute of Environmental Physics, University of Heidelberg (2007).

[Rus1] D Russo. Determining soil hydraulic properties by parameter estimation: On the selection of a model for the hydraulic properties, *Wat. Resour. Res.* **24(3)** (1988) 453459.

[San1] P Sánchez, S Ahamed, F Carré, A Hartemink, J Hempel, J Huising, P Lagacherie, A McBratney, N McKenzie, M Mendonça-Santos, B Minasny, L Montanarella, P Okoth, C Palm, J Sachs, K Shepherd, T Våagen, B Vanlauwe, M Walsh, L Winowiecki, GL Zhang. Digital Soil Map of the World. *Science.* **325** (2009) 680-681.

[Sak1] R Saksena, S Chandra and BP Singh. A gamma transmission method for the determination of moisture content in soils. *J. Hydrol.* **23** (1974) 341-362.

[Sch1] WM Schuh and RL Cline, Effect of soil properties on unsaturated hydraulic conductivity pore-interaction factors, *Soil Sci. Soc. Am. J.* **54** (1990) 15091518.

[Sch2] MG Schaap and FJ Leij, Improved prediction of unsaturated hydraulic conductivity with the Mualem-van Genuchten model, *Soil Sci. Soc. Am. J.* **64** (200) 843851.

[Sch3] C Schlichter. Principles of Magnetic Resonance. Springer-Verlag. Heidelberg-New York. 1990.

[Sch4] B Scharnagl. Determination of Soil Hydraulic Properties from Multi-Step Outflow Experiments on the Laboratory and Lysimeter Scale. Diplomarbeit. TU Braunschweig (2006).

[See1] R Seemann, M Brinkmannm and S Hemminghaus, Auf Sand gebaut, *Physik Journal* **8** (2009) Nr. 11 31-36.

[Sha1] S Sharma, F Casanova, W Wache, AL Segre and B Blümich. Analysis of historical porous building materials by the NMR-MOUSE® *Mag. Res. Imaging.* **21** (2003) 249-255.

[Šim1] Šimůnek, J., Šejna M., and van Genuchten., M. T., 2008. The HYDRUS-1D software package for simulating the one-dimensional movement of water, heat, and multiple solutes in variably saturated media, version 2.0, U.S. Salinity Lab. Agric. Res. Serv. Riverside CA (USA), 2008

[Son1] Y Song. Resolution and uncertainty of Laplace inversion spectrum. *Magn. Reson. Imag.* **25** (2007) 445-448.

[Sti1] Stingaciu L, Pohlmeier P, Blümler P, Weihermüller L, van Dusschoten D, Stapf S and Vereecken H. Characterization of unsaturated porous media by high field and low field NMR relaxometry. *Water Resour. Res.* **45** (2009) W08412.

[Sui1] BH Suits, AN Garroway and JB Miller. Noise-Immune coil for unshielded magnetic resonance measurements, *J. Magn. Reson.* **131** (1998) 154-158.

[TR32, 2010] Interdisciplinary Collaborative Research Center TR32. Patterns in the soil-vegetation-atmospheric system: monitoring, modeling, data assimilation. Funded by the Deutsche Forschungsgemeinschaft, DFG. 21, Jan, 2010, Available from: www.tr32.de.

[Van1] M Van Genuchten. A closed-form equation for predicting the hydraulic conductivity of unsaturated soils. *Soil Sci. Soc. Am. J.* **44** (1980) 892-898.

[Wei1] W Weibull. A statistical distribution of wide applicability. *J. Appl. Mech. Trans. ASME* **18(3)** (1951) 293-197.

[Wei2] L Weihermüller, JA Huisman, S Lambot, M Herbst, H Vereecken. Mapping the spatial variation of soil water content at the field scale with different ground penetrating radar techniques. *J. Hydrol.* **340** (2007) 205216.

[Zac1] DW Zachmann, PC DuChateau and A Klute. Simultaneous approximation of water capacity and soil hydraulic conductivity by parameter identification, *Soil Science* **134** (1982) 157163.

[Zur1] Y Zur. An algorithm to calculate the NMR signal of a multi spin-echo sequence with relaxation and spin-diffusion. *J. Magn. Reson.* **171** (2004) 97-106.

Danksagung

Es gibt selbst verständlich einige Menschen und Institutionen, die mich in dieser wissenschaftliche Abenteuer fachlich und menschlich begleiten haben. Deswegen bedanke ich mir ganz herzlich bei

- Prof. Bernhard Blümich für seine vorbehaltlose Betreuung, durch die es mir klar wurde, dass die wissenschaftliche Arbeit sich vor allem nach konkrete Ergebnisse orientieren muss und für die Gelegenheit, die unerschöpfbaren Möglichkeiten der Kernresonanz kennenzulernen.

- Andreas Pohlmeier, dessen fachlicher Betreuung in einer entscheidenden Moment auftauchte und sich hoch kompetent und grosszügig erwies.

- Prof. Stephan Appelt für seine hervorrangende Vorlesungen, mit denen er uns eine ganz hilfsreich Überblick auf der Theorie der Kernresonanz übermittelt hat. Dabei zu sitzen war wirklich wie "Vor der Tiefe des Meeres bevorzustehen", wie es einmal Newton formulierte.

- Meinen Forschungsstudenten: Daniela Jhon, Martin Dabrowski und Adrien Miníere, die nicht nur eine grosse Hilfsarbeit geleistet sondern auch mit ihrem Lernbegierde jugenliches Entusiasmus in unseren Labor "hingegossen" haben

- Einigen Kollegen, die auch durch ihre Gespräche und einfach freundliche Anwesenheit meine Aufenthalt in Deutschland menschlich bereichert haben: Nico Goga, Cladiu Melian, Natasha Spindler, Jörg Mauler und Romualdo Ferreyra. Herzliche Danke an euch alle!.

- Die technische Angelegenheiten, die immer zu einer echten Herausförderung werden können, hätte ich nicht ohne die Hilfe von Ing. Michael Adams und Klaus Kupferschläger uberwältigen können. Herzliche Danke an euch beide.

- Der Deutscher Akademischer Austausch Dienst (DAAD) für die finazielle Förderung, die mein Studium in diesem Land möglicht machte.

- Meine Eltern, die mich so viel gegeben haben, ohne etwas verlangt zu haben.

- und meine Frau Olga Surikova. Ohne deine Begleitung, Geduld und Unterstützung wäre es nie möglich gewesen.

Lebenslauf

Name:	Sucre Reyes
Vorname:	Oscar Elías
Geburstag:	30 Juni 1975.
Geburtsort:	Baruta, Venezuela.
Staatsangehörigkeit:	Venezolanische

Qualifikationen

1987-1992	Abitur, IEAH, Maturín, Venezuela.
1992-1998	Dip. Phys. an der USB, Caracas, Venezuela.
2001-2006	Ms. Sc. an der UCV, Caracas, Venezuela.
2006-2010	Promotion an der RWTH Aachen, Aachen, Deutschland.

Berufliche Tätigkeit

2000-2001	Technische Hilfskraft bei Técnica Spadoni C.A. Caracas, Venezuela.
2001-2006	Physiklehrer bei der Universidad de Carabobo, Valencia, Venezuela.